



Origin of star-forming rings around massive centres in massive galaxies at $z < 4$

Avishai Dekel,^{1,2*} Sharon Lapiner,¹ Omri Ginzburg,¹ Jonathan Freundlich^{1,3}, Fangzhou Jiang^{1,4}, Bar Finish,¹ Michael Kretschmer^{1,3}, Doug Lin,⁴ Daniel Ceverino^{1,5}, Joel Primack,⁶ Mauro Giavalisco⁷ and Zhiyuan Ji⁷

¹Racah Institute of Physics, The Hebrew University, Jerusalem 91904, Israel

²SCIPP, University of California, Santa Cruz, CA 95064, USA

³Institute for Computational Science, University of Zurich, CH-8057 Zurich, Switzerland

⁴Department of Astronomy and Astrophysics, University of California, Santa Cruz, CA 95064, USA

⁵Departamento de Física Teórica, Facultad de Ciencias, Universidad Autónoma de Madrid, Cantoblanco, E-28049 Madrid, Spain

⁶Physics Department, University of California, Santa Cruz, Santa Cruz, CA 95064, USA

⁷Department of Astronomy, University of Massachusetts, Amherst, MA 01002, USA

Accepted 2020 June 11. Received 2020 June 10; in original form 2020 March 18

ABSTRACT

Using analytic modelling and simulations, we address the origin of an abundance of star-forming clumpy extended gas rings about massive central bodies in massive galaxies at $z < 4$. Rings form by high-angular-momentum streams and survive in galaxies of $M_{\text{star}} > 10^{9.5-10} M_{\odot}$ where merger-driven spin flips and supernova feedback are ineffective. The rings survive after events of compaction to central nuggets. Ring longevity was unexpected based on inward mass transport driven by torques from violent disc instability. However, evaluating the torques from a tightly wound spiral structure, we find that the time-scale for transport per orbital time is long and $\propto \delta_d^{-3}$, with δ_d the cold-to-total mass ratio interior to the ring. A long-lived ring forms when the ring *transport* is slower than its replenishment by *accretion* and the interior *depletion* by star formation rate, both valid for $\delta_d < 0.3$. The central mass that lowers δ_d is a compaction-driven bulge and/or dark matter, aided by the lower gas fraction at $z < 4$, provided that it is not too low. The ring is Toomre unstable for clump and star formation. The high- z dynamic rings are not likely to arise from secular resonances or collisions. Active galactic nucleus feedback is not expected to affect the rings. Mock images of simulated rings through dust indicate qualitative consistency with observed rings about bulges in massive $z \sim 0.5-3$ galaxies, in H α and deep *HST* imaging. ALMA mock images indicate that $z \sim 0.5-1$ rings should be detectable. We quote expected observable properties of rings and their central nuggets.

Key words: galaxies: discs – galaxies: evolution – galaxies: formation – galaxies: haloes – galaxies: mergers – galaxies: spirals.

1 INTRODUCTION

High-redshift galaxies are predicted to be fed by cold gas streams from the cosmic web (Birnboim & Dekel 2003; Kereš et al. 2005, 2009; Dekel & Birnboim 2006; Dekel et al. 2009a). According to cosmological simulations, these streams enter the dark matter (DM) halo with high angular momentum (AM), which they lose in the inner halo and spiral in into an extended gas ring (Danovich et al. 2015), as seen in Fig. 1.

This ring, like the inner disc, is at a constant risk of being disrupted by a major merger of galaxies at nodes of the cosmic web, which typically involves a change in the pattern of AM-feeding streams. In Dekel et al. (2020), we showed that in haloes below a critical virial mass of $M_v \sim 10^{11} M_{\odot}$, the merger-driven spin flips are indeed disruptive as they tend to be gas rich and more frequent than the disc/ring orbital frequency. In more massive haloes, the mergers are less frequent, thus possibly allowing the rings/discs to survive for many orbital times. The additional disruptive effects of supernova

feedback, which could be strong below a similar critical mass where the potential well is shallow compared to the energy deposited by supernovae in the interstellar medium (ISM; Dekel & Silk 1986), are also expected to be weak above this threshold mass, where the gas binding energy is higher.

Another process that could in principle disrupt discs even above the mass threshold is the inward mass transport associated with violent disc instability (VDI). When the gas fraction is high, and the bulge is not massive, this process has been estimated to be efficient, such that the disc or ring was expected to be evacuated inwards in a few orbital times (Noguchi 1999; Immeli et al. 2004; Bournaud, Elmegreen & Elmegreen 2007; Genzel et al. 2008; Dekel, Sari & Ceverino 2009b). In contrast, as we will see below, the simulations (indicated already in Ceverino, Dekel & Bournaud 2010; Genel et al. 2012), and observations (below and in Section 6.2), show many long-lived rings in massive galaxies, thus posing a theoretical puzzle that is our main concern here.

Related to this is the phenomenon of wet compaction into a blue nugget (BN), which tends to occur in most galaxies near a characteristic mass of a similar value (Zolotov et al. 2015; Tacchella et al. 2016a, b; Tomassetti et al. 2016; Dekel, Lapiner & Dubois

* E-mail: avishai.dekel@mail.huji.ac.il

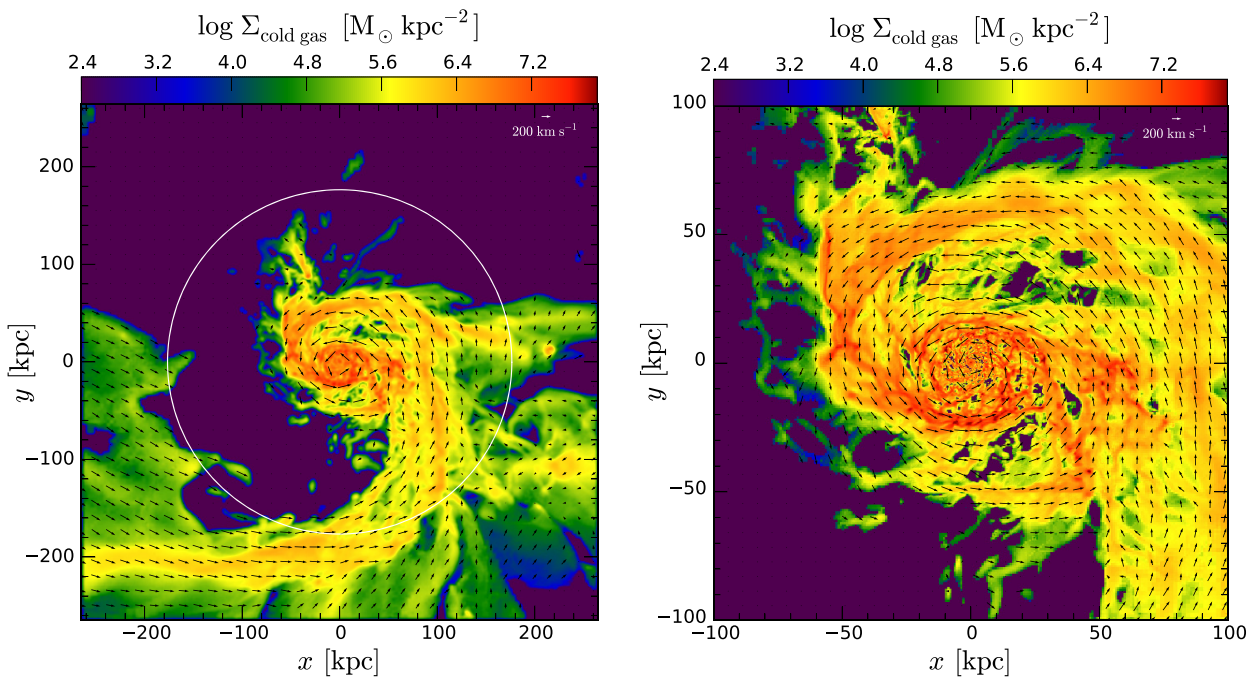


Figure 1. Ring buildup by a high-angular-momentum (AM) stream from the cosmic web. Shown is the face-on projected gas density (colour) in a VELA simulated galaxy (V07 at $z = 1.08$) and the 2D velocity field (arrows). The virial radius is marked by a white circle. Left: Zoom-out on the stream extending out to > 300 kpc with an initial impact parameter comparable to the virial radius. Right: Zoom-in on the spiralling-in to a ring at $\sim 10 - 20$ kpc. As illustrated in a cartoon in fig. 20 of Danovich et al. (2015), the AM gained outside the halo by tidal torques from the cosmic web is gradually lost in the inner halo by torques from friction, other streams and the tilted disc, causing the buildup of a ring. The question is what prevents the ring from contracting further.

2019b). This process is sometimes driven by mergers and in other times by other mechanisms such as counter-rotating streams. The BNs are observed as compact star-forming galaxies at $z \sim 1 - 3$ (e.g. Barro et al. 2017a), with a preferred stellar mass of $M_s \sim 10^{10} M_\odot$ (Huertas-Company et al. 2018). We learn from the simulations that the rings tend to form and survive especially after a compaction event, namely above the threshold mass. *The way the compaction could give rise to a ring and stabilize it against inward mass transport is the main issue addressed here.* We study below the ring survival by analysing the torques exerted by a spiral structure. We find that the post-compaction massive bulge could be the main reason for slowing down the mass transport while keeping the ring Toomre unstable for giant clumps and star formation. By comparing the inward transport rate of the ring to its replenishment by external accretion and the interior depletion to star formation, we work out the conditions for ring formation and longevity.

In parallel to our analytic modelling, we utilize a suite of VELA zoom-in hydro-cosmological simulations, which are described in Appendix A and Table A1 (available in the Supporting Information) and in earlier papers (e.g. Ceverino et al. 2014; Zolotov et al. 2015; Dekel et al. 2019a, 2020). Here, we bring only a brief summary of the relevant features of these simulations. The simulations are based on the Adaptive Refinement Tree code (Kravtsov, Klypin & Khokhlov 1997; Ceverino & Klypin 2009). The suite consists of 34 galaxies that were evolved to $z \sim 1$, with a unique maximum spatial resolution ranging from 17.5 to 35 pc at all times. The DM halo masses at $z = 2$ range from 10^{11} to $10^{12} M_\odot$, thus avoiding dwarf galaxies at $z < 4$. The galaxies were selected at $z = 1$ such that their DM haloes did not suffer a major merger near that epoch, which turned out to eliminate less than 10 percent of the haloes.

Besides gravity and hydrodynamics, the code incorporates physical process relevant for galaxy formation such as gas cooling by atomic hydrogen and helium, metal and molecular hydrogen cooling, photoionization heating by the UV background with partial self-shielding, star formation, stellar mass loss, metal enrichment of the ISM, and stellar feedback. Supernovae and stellar winds are implemented by local injection of thermal energy, and radiation-pressure stellar feedback is implemented at a moderate level. In general, the feedback as implemented in this suite is on the weak side of the range of feedback strengths in common cosmological simulations, and no active galactic nucleus (AGN) feedback is incorporated.

In the analysis of the simulations, the disc plane and dimensions are determined iteratively, as detailed in Mandelker et al. (2014), yielding a disc radius R_d and half-height H_d (listed at $z = 2$ in Table A1 in Appendix A, available in the Supporting Information) that contain 85 per cent of the cold ($T < 1.5 \times 10^4$ K) gas mass out to $0.15 R_v$, where R_v is the halo virial radius. The level of ‘disciness’ is measured by the kinematic ratio of rotation velocity to velocity dispersion V_{rot}/σ , or similarly by R_d/H_d . Rings are identified and their properties are quantified as described in Section 3.3 and in Appendix B (available in the Supporting Information). Mock images of simulated galaxies as observed through dust are generated (based on Snyder et al. 2015a) for a preliminary comparison to galaxies observed in deep fields of the *Hubble Space Telescope (HST)-CANDELS* survey. Corresponding mock ALMA images are also generated and mock H_α properties are computed.

There are robust observational detections in H_α for abundant star-forming rings about massive central bodies at $z \sim 1 - 2$ (Genzel et al. 2014, 2017, 2020), which seem to be qualitatively matched by the simulated rings described here. Furthermore, contrary to earlier

impressions from *HST*-CANDELS images, similar star-forming rings about massive bulges are being detected in non-negligible abundances in massive galaxies at $z \sim 0.5\text{--}3$ when properly focusing on the deepest fields (Ji et al., in preparation). Possibly related is the abundance of rings about massive bulges in low-redshift S0 galaxies entering the ‘Green Valley’ (Salim et al. 2012), also beautifully seen in IR images of nearby galaxies with massive bulges such as M31 and the Sombrero galaxy. Towards the end of this paper, we attempt very preliminary comparisons between the theoretical and observed high- z rings, and quote certain predicted observable ring properties for more rigorous comparisons with observations, to be performed beyond the scope of this theory paper.

The paper is organized as follows. In a second introductory section, Section 2, we elaborate on the formation of rings from the cosmic-web streams, the threshold mass for long-lived discs/rings due to merger-driven spin flips, and the expected disc disruption by inward mass transport driven by VDI. In Section 3 we demonstrate using the simulations the effect of compaction to a BN on the generation of long-lived extended discs and then rings above the threshold mass. In particular, in Section 3.3, we quantify the ring properties and demonstrate their correlation with the compaction events. In Section 4, *the heart of this paper*, we attempt to understand the stabilization of an extended ring by a massive central body via an analytic derivation of the torques exerted on the ring by a perturbed disc with a tightly wound spiral-arm structure. The condition for a long-lived ring is evaluated by comparing the inward transport rate to the rates of accretion and star formation in Section 4.2, and the model is tested against the simulations in Section 4.5. In Section 6 we make first steps of comparing the simulated rings to observations, where we show example mock images and the corresponding profiles from the simulations, both in the *HST* bands and for ALMA, and show a sneak preview of rings plus bulges detected in deep CANDELS fields. In Section 8 we summarize our conclusions. Certain more technical matters are deferred to appendices (available in the Supporting Information). In the appendices (available in the Supporting Information) we describe the VELA simulations (Appendix A), elaborate on how we measure ring properties and present the distributions of certain properties (Appendix B), evaluate the possible torques from a prolate central body (Appendix C), and bring complementary images of rings in the simulations and observations (Appendix D).

2 RING FORMATION

This more detailed introductory section elaborates on the background and motivation for the analysis of compaction-driven rings and their longevity.

2.1 Ring formation from cosmic-web streams

The buildup of an extended ring is a natural result of the feeding of high-redshift galaxies by streams of cold gas that ride the DM filaments of the cosmic web into its nodes. At sufficiently high redshifts, even in massive haloes the streams can penetrate cold through the halo virial radius without being heated by a stable virial shock because their higher density induces efficient post-shock cooling that does not allow pressure support for the shock against gravitational collapse (Birnboim & Dekel 2003; Kereš et al. 2005; Dekel & Birnboim 2006; Cattaneo et al. 2006; Ocvirk, Pichon & Teyssier 2008; Dekel et al. 2009a; Kereš et al. 2009; Danovich et al. 2012). The evolution of cold-gas AM leading to the buildup of a ring is described in four stages in Danovich et al. (2015), as summarized in a cartoon in their fig. 20. Fig. 1 demonstrates the buildup of a

ring by a high-AM stream, focusing on one dominant stream in an example galaxy from the VELA suite of zoom-in cosmological simulations. The streams acquire excessive AM by tidal torques from the cosmic web while outside the halo (White 1984), expressed in terms of a velocity comparable to the virial velocity and an impact parameter that could be on the order of the virial radius. As the stream penetrates into the halo it spirals in and settles into an extended ring at $\sim 0.15R_v$. The significant AM loss is by torques due to friction against the circum-galactic medium (CGM) and disc gas as well as by torques from the central galaxy and other streams. As the virial radius is growing with time, the initial impact parameter and the resultant ring radius become more extended in time. Results of related nature were obtained from other simulations (Pichon et al. 2011; Codis et al. 2012; Stewart et al. 2013).

Preliminary observational kinematic studies of cold gas, via Ly α absorption along the line of sight to a background quasar, or Ly α emission that is typically stimulated by a nearby quasar, indeed indicate detections of cold inflowing gas with high AM, consistent with the simulation predictions (e.g. Martin et al. 2019). A recent observed system at $z = 2.9$, that is not illuminated by a nearby quasar, also indicates three cold inflowing streams (Daddi et al., in preparation).¹ These observations provide preliminary confirmation for the natural buildup of an extended ring, as seen in the simulations.

2.2 Mass threshold for discs by merger-driven spin flips

The extended rings that form are expected to be fragile. In Dekel et al. (2020) we used the simulations and analytic estimates to explore how discs and rings populate the M_v – z plane. The disc disruption below a characteristic mass is shown in Fig. 2, which displays the distribution of a kinematic measure of gas disciness, V_{rot}/σ , in the VELA simulations. On the left, this ratio (colour) is averaged over the simulation snapshots in bins of M_v and z . On the right, this ratio is shown as a function of halo mass for every snapshot. We see a systematic gradient of disciness with mass, and a division between the zones of non-disc and disc dominance at a critical mass of $M_v \simeq (1\text{--}2) \times 10^{11} M_\odot$, where $V_{\text{rot}}/\sigma \simeq 2$. No significant redshift dependence is seen. A measure of disciness by shape reveals similar results, with a transition at $R_d/H_d \simeq 2.5$.

In particular, major mergers are expected to disrupt rotation-supported systems if the orbital AM and the spin of the merging galaxy are not aligned with the spin of the galaxy. This is expected to be the case in mergers of high-sigma nodes of the cosmic web, when the pattern of feeding streams drastically changes. Figs 4 and 5 of Dekel et al. (2020) demonstrate that the disruption below the critical mass is largely due to merger-driven spin flips in less than an orbital time. The mass threshold is derived by a simple analytic model, contrary to the naive expectation of a redshift threshold based on halo merger rates, where the time between mergers with respect to the halo orbital time is $t_{\text{mer}}/t_{\text{orb}} \propto (1+z)^{-1}$ (Neistein & Dekel 2008; Dekel et al. 2013). This turns into a mass threshold when taking into account the increase of the ratio of baryonic galaxy mass to its halo mass with mass and redshift. While the external inflow (and

¹In two of these streams the line-of-sight velocity is decreasing from large projected radii towards the centre and even reversing its sign along the way. Rather than interpreting this as a deceleration of the stream as it falls in, this behaviour is consistent with viewing an in-spiralling stream similar to the one shown in Fig. 1 from the left or the right, where the velocity becomes perpendicular to the line of sight as the stream enters the inner halo, and it may even reverse its line-of-sight velocity on the other side of the central galaxy.

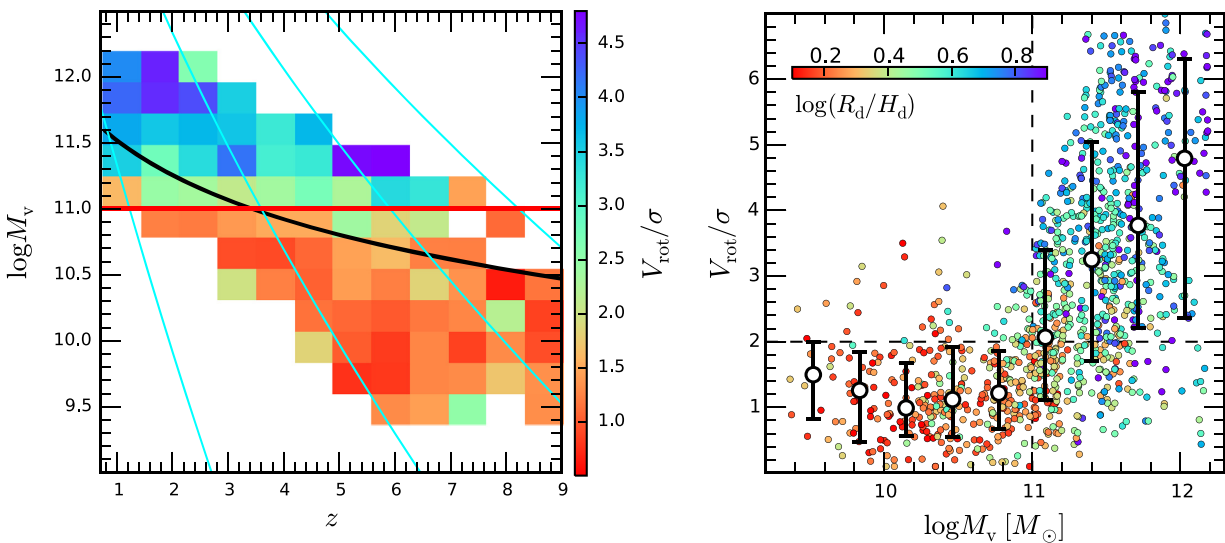


Figure 2. Disc disruption below a characteristic mass. Shown is the degree of disciness in terms of V_{rot}/σ in the VELA simulations. Left: V_{rot}/σ (colour) is averaged within bins in the mass–redshift plane. The black curve refers to the upper limit for effective supernova feedback at a virial velocity $V_v = 120 \text{ km s}^{-1}$. The cyan curves refer to the Press-Schechter $\nu\sigma$ peaks, for $\nu = 1, 2, 3, 4$ from left to right, respectively. Right: V_{rot}/σ as a function of halo mass M_v for all the snapshots of all the 34 evolving galaxies. Each point refers to a snapshot, with the median and 1σ scatter (16 and 84 per cent percentiles) marked in bins of M_v . The colour refers to the alternative measure of disciness by shape using R_d/H_d , showing consistency between the two alternative measures of disciness. In both figures we see a marked transition from non-discs to discs or rings at a threshold mass of $M_v \simeq 10^{11} M_\odot$, with negligible redshift dependence, as predicted analytically in Dekel et al. (2020).

merger) rate of mass and AM that could damage a disc is primarily determined by the total halo mass, the AM of the existing central galaxy that it is affecting is increasing with its baryonic mass, so the damaging relative change in AM is expected to be larger for lower-mass galaxies and at lower redshifts. This introduces a strong mass dependence in the disc survivability and weaken its redshift dependence, as seen in the simulations.

We thus learn in Dekel et al. (2020) that above a threshold mass the discs and rings are expected not to suffer disruptions by merger-driven spin flips on time-scales comparable to their orbital times.

Given this threshold mass, the expected abundance of gas discs/rings in a given redshift can be estimated by the number density of haloes above the threshold mass. For the LCDM cosmology the Press-Schechter formalism yields a comoving number density of $n > 10^{-2} \text{ Mpc}^{-3}$ in the redshift range $z = 0\text{--}2$, and $n > 2.8 \times 10^{-3}, 5.2 \times 10^{-4}, 3.2 \times 10^{-5} \text{ Mpc}^{-3}$ at $z \simeq 4, 6, 10$ respectively.

2.3 Rapid inward mass transport driven by violent disc instability

In addition to mergers, another risk for the long-term survival of an extended disc or ring is the inward mass transport associated with VDI. In a gravitationally unstable gas disc, the non-cylindrically symmetric density perturbations exert torques on the rest of the disc, which typically cause transport of AM outward. Then, AM conservation, or the angular Euler equation (equation 6.34 of Binney & Tremaine 2008, hereafter BT), implies an associated mass transport inward, in terms of clump migration and gas inflow through the disc (e.g. Noguchi 1999; Gammie 2001; Bournaud et al. 2007, 2011; Elmegreen, Bournaud & Elmegreen 2008; Dekel et al. 2009b; Ceverino et al. 2010, 2012; Forbes, Krumholz & Burkert 2012; Goldbaum, Krumholz & Forbes 2015, 2016).

Considering mutual encounters between the giant clumps in a VDI disc, Dekel et al. (2009b, equation 21) evaluated the evacuation time

of the disc to be

$$t_{\text{inf}} \simeq 1.7 \alpha_{0.2}^{-1} Q^2 \delta_d^{-2} t_{\text{orb}}, \quad (1)$$

where $\alpha = 0.2\alpha_{0.2}$ is the instantaneous fraction of the cold disc mass in clumps and $Q \sim 1$ is the Toomre parameter. The most meaningful variable here is δ_d , the mass ratio of cold disc to total mass within the sphere of radius r where the time-scale is evaluated,

$$\delta_d \equiv \frac{M_d}{M_{\text{tot}}}. \quad (2)$$

The disc mass M_d refers to the ‘cold’ mass that participates in the gravitational instability. In principle it includes the cold gas and the young stars, but it can be approximated to within a factor of two by the cold gas, as the young stars typically contribute about half of the gas mass. The total mass includes also the ‘hot’ stars in the disc and bulge and the DM mass within r . This quantity, δ_d , will turn out to also play a major role in our analytical modelling of rings in Section 4 below.

An alternative estimate of the inflow time has been obtained in Dekel et al. (2009b, equation 24) based on the shear-driven mass-inflow rate of Shakura & Sunyaev (1973) and the maximum dimensionless AM flux density $\tilde{\alpha}$ obtained from simulations by Gammie (2001), yielding a lower limit of

$$t_{\text{inf}} \sim 1.2 Q^{-2} \delta_d^{-2} t_{\text{orb}}. \quad (3)$$

With Q between unity and 0.68, appropriate for marginal instability of a thick disc (Goldreich & Lynden-Bell 1965), this is comparable to the estimate in equation (1) despite the opposite dependence on Q .

In a VDI disc with $\delta_d \sim 0.3\text{--}0.5$, we thus expect an inward mass transport within a few orbital times. With such a rapid inflow rate, one would not expect the extended discs to survive for a long time the way they do for massive, post-compaction galaxies in the simulations (see below). This is given that the expected average time-

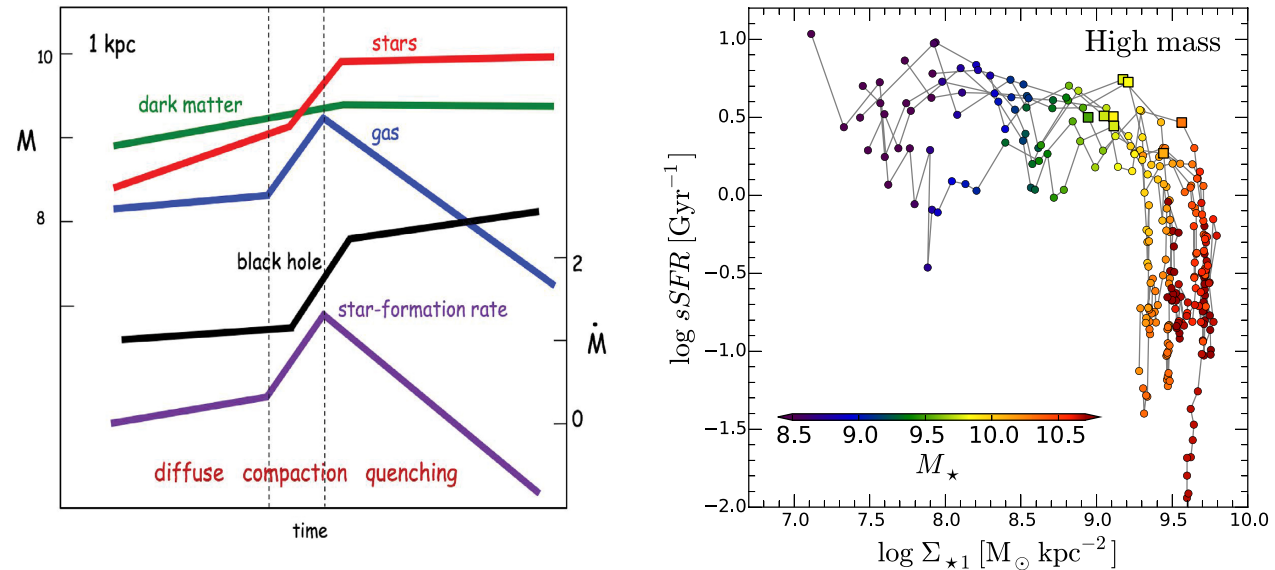


Figure 3. Compaction to a blue nugget (BN) and quenching in cosmological simulations. Left: A cartoon describing a typical wet-compaction event (see images in Fig. 4), showing the evolution of masses (in $\log(M/M_\odot)$) within the inner 1 kpc (following Zolotov et al. 2015). The compaction is the steep rise of gas mass (blue), by an order of magnitude during $\sim 0.3 t_{\text{Hubble}}$, reaching a peak as a BN, and soon after declining as the central gas is depleted by star formation and outflows with no replenishment. The SFR (magenta, in $\log(M_\odot \text{ yr}^{-1})$) follows closely, demonstrating post-BN compaction-triggered central quenching. The central stellar mass (red) is rising accordingly during the compaction, and it flattens off post-BN. The inner 1 kpc is dominated by dark matter (green) pre-compaction and by baryons (stars, red) post-compaction. The ‘disc’ kinematics is dispersion-dominated pre-BN and rotation-dominated post-BN (Fig. 7). The time of the major BN event is typically when the galaxy is near the golden mass, $M_s \sim 10^{10} M_\odot$, separating between the pre-compaction supernova phase and the post-compaction hot-CGM phase. The black hole growth (black), which is suppressed by supernova feedback pre-compaction, is growing during and after the compaction in the hot-CGM phase above the golden mass. The onset of rapid black hole growth is driven by the compaction event (Dekel et al. 2019b). Right: The universal L-shape evolution track of eight VELA simulated galaxies in the plane of sSFR and stellar surface density within 1 kpc, Σ_1 , which serves as a measure of compactness (following Lapiner, Dekel et al., in preparation). The compactness is growing at a roughly constant sSFR (horizontally) before and during the compaction event, turning over at the BN phase (the ‘knee’, marked by a square symbol) to quenching at a constant Σ_1 (vertically). A similar behaviour is seen observationally (Barro et al. 2017a, fig. 7), with the value of Σ_1 at the BN phase weakly increasing with redshift. Note that this phenomenon is not caused by AGN feedback.

scale for accretion into the ring is much longer, $t_{\text{acc}} \sim 20(1+z)^{-1}t_{\text{orb}}$, as estimated in equation (27) below. This puzzling low inflow rate of the post-compaction rings in the simulated galaxies has been a long-standing theoretical challenge, which we seek to solve here. It turns out that the same quantity, δ_d , will play a major role also in our analytical modelling of rings in Section 4.

3 POST-COMPACTATION DISCS AND RINGS IN SIMULATIONS

The mass threshold for survival of discs and rings, which we interpreted in Dekel et al. (2020) as largely due to merger-driven spin flips on an orbital time-scale, is apparently associated with another physical process that tends to occur near a similar characteristic mass, that of a major compaction event. We describe here how long-lived discs and rings tend to appear in the simulations after such a compaction event, once a massive bulge has formed.

3.1 Compaction to a blue nugget

Cosmological simulations show that most galaxies evolve through a dramatic wet-compaction event, which tends to occur at its maximum strength when the galaxy mass is near or above the golden value, $M_v \sim 10^{11.5} M_\odot$ and $M_s \sim 10^{9.5} M_\odot$, especially at $z = 1-5$ when the gas fraction is high (Zolotov et al. 2015; Tacchella et al. 2016b; Tomassetti et al. 2016; Dekel et al. 2019b). The wet compaction is a

significant gaseous contraction into a compact central star-forming core within the inner 1 kpc, termed ‘a BN’. The gas consumption by star formation and the associated gas ejection by stellar and supernova feedback trigger central gas depletion and inside-out quenching of star formation rate (SFR; Tacchella et al. 2016a). The cartoon in Fig. 3 illustrates the main features of this sequence of events as seen in the simulations via the evolution of gas mass, stellar mass and SFR within the inner kiloparsec. The compaction is identified in each simulated galaxy primarily by the peak in gas mass within 1 kpc that is followed by a significant depletion. Secondary tracers of compaction are the end of the steep rise in stellar mass within 1 kpc where it turns into a plateau, and the transition from central DM dominance to baryon dominance. In order to more directly compare to observations, the right-hand panel of Fig. 3 shows simulated evolution tracks of galaxies in the plane of specific SFR (sSFR) versus compactness as measured by the stellar surface density within 1 kpc, termed Σ_1 . A compaction at a roughly constant sSFR turns into quenching at a constant Σ_1 , generating an L-shape evolution track with the ‘knee’ marking the BN phase. This characteristic L-shape evolution track has been confirmed observationally (e.g. Barro et al. 2017a, fig. 7). Fig. 4 illustrates through images of gas and stellar surface density the evolution through the compaction, BN and post-BN phases in an example VELA galaxy (V07), to be discussed below. Fig. D1 in Appendix D (available in the Supporting Information) brings a more detailed sequence of the evolution.

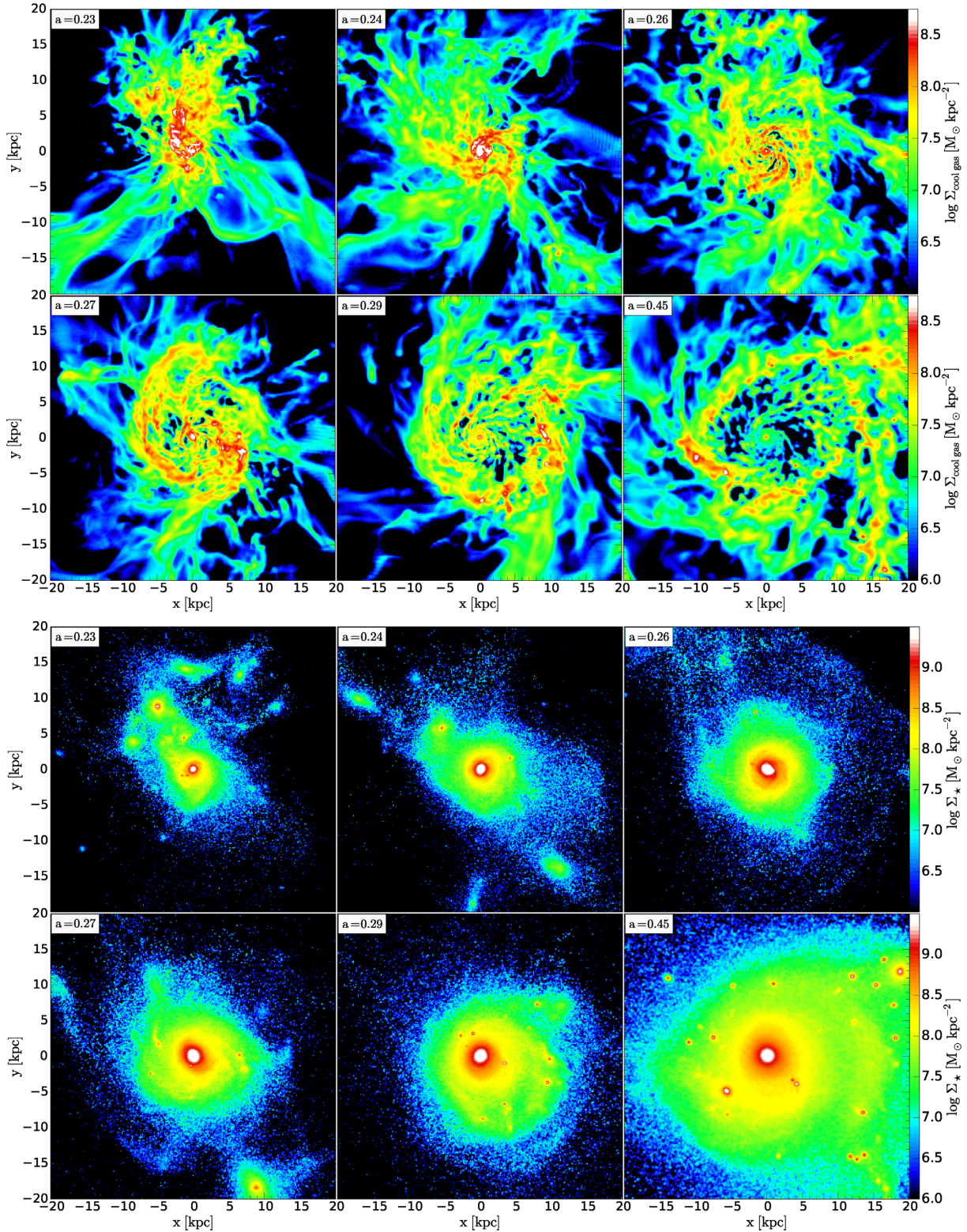


Figure 4. Compaction to a blue nugget and post-compaction gas disc and ring surrounding a massive compact bulge. Shown are the projected densities of gas (top) and stars (bottom) in different phases [expansion factor $a = (1 + z)^{-1}$ is marked] during the evolution of one of the VELA simulated galaxies (V07). The projections are face on with respect to the AM. From top to bottom, left to right. First: during the compaction process ($\log M_s = 10.0$, $\log M_v = 11.6$). Second: at the BN phase (10.3, 11.7). Third and fourth: post-compaction VDI disc (10.5, 11.8). Fifth and sixth: post-compaction clumpy long-lived ring, fed by incoming streams (10.8, 12.1). The stellar compact red nugget forms during and soon after the compaction and the resulting bulge remains compact and grows massive thereafter.

Observationally, it became evident that the massive passive galaxies, which are already abundant at $z \sim 2$ –3, are typically compact, encompassing $\sim 10^{10} M_{\odot}$ of stars within 1 kpc, termed ‘red nuggets’ (van Dokkum et al. 2008, 2010, 2014, 2015; Damjanov et al. 2009, 2011; Newman et al. 2010; Bruce et al. 2012; Whitaker et al. 2012). Their effective radii are typically 1 per cent of their halo virial radii, which is smaller than one would expect had the gas started in the halo with a standard spin of $\lambda \sim 0.035$ and conserved AM during the infall. This indicates dissipative inflow associated with AM loss, namely a wet compaction (Dekel & Burkert 2014), and it implies the presence of gaseous BNs as the immediate progenitors of the red nuggets. Indeed, star-forming BNs have been convincingly observed, with masses, structure, kinematics and abundance consistent with being the progenitors of the red nuggets (Barro et al. 2013, 2014a, b; Williams et al. 2014; Barro et al. 2015; van Dokkum et al. 2015; Williams et al. 2015; Barro et al. 2016b, a, 2017b, a). In particular, a machine-learning study, after being trained on mock dusty images of the BNs as identified in the simulations, recognized with high confidence similar BNs in the CANDELS-*HST* multicolour imaging survey of $z = 1$ –3 galaxies (Huertas-Company et al. 2018). The comoving number density of BNs at $z \sim 2$ is estimated to be $n \sim 2 \times 10^{-4} \text{ Mpc}^3$ both in the simulations and in the observations (Barro et al. 2017a).

The AM loss leading to compaction is found in the simulations to be caused either by wet mergers (~ 40 per cent by major plus minor mergers), by colliding counter-rotating streams, by recycling fountains or by other processes (in preparation), and to be possibly associated with VDI (Dekel & Burkert 2014). These processes preferentially occur at high redshifts, where the overall accretion is at a higher rate and more gaseous, leading to deeper compaction events.

The compaction events mark drastic transitions in the galaxy structural, compositional, kinematic and other physical properties, which translate to pronounced changes as a function of mass near the characteristic mass for major BNs (Zolotov et al. 2015; Tacchella et al. 2016a, b). The compaction triggers inside-out quenching of star formation, to be maintained by a hot CGM in massive haloes, possibly aided by AGN feedback. This is accompanied by a structural transition from a diffuse and largely amorphous configuration to a compact system, possibly surrounded by an extended gas-rich ring and/or a stellar envelope. The kinematics evolves accordingly from pressure to rotation support (Fig. 7 below). Due to the compaction, the central region turns from DM dominance to baryon dominance, which induces a transition of global shape from a prolate to an oblate stellar system (Ceverino, Primack & Dekel 2015; Tomasetti et al. 2016) consistent with observations (Zhang et al. 2019). Finally, the BN marks a transition in the central black hole growth rate from slow to fast (Dubois et al. 2015; Anglés-Alcázar et al. 2017; Bower et al. 2017; Habouzit et al. 2019; Dekel et al. 2019b), which induces a transition from supernova feedback to AGN feedback as the main source for quenching of star formation.

Especially important for our purpose here is that the BNs favour a characteristic mass. According to the simulations, minor compaction events may occur at all masses in the history of a star-forming galaxy (SFG). Indeed, repeated episodes of minor compactions and subsequent quenching attempts can explain the confinement of SFGs to a narrow main sequence (Tacchella et al. 2016b). However, the major compaction events, those that involve an order-of-magnitude increase in central density, cause a transition from central DM dominance to baryon dominance, and trigger significant and long-lasting quenching, are predicted by the simulations to occur near a characteristic halo mass about $M_v \sim 10^{11.5} M_{\odot}$, see Tomasetti

et al. (2016, fig. 8) and Zolotov et al. (2015, fig. 21). This has been confirmed by the deep-learning study of VELA simulations versus observed CANDELS galaxies (Huertas-Company et al. 2018), which detected a preferred stellar mass for the observed BNs near the golden mass, $M_s \sim 10^{9.5-10} M_{\odot}$. The significance of this finding is strengthened by the fact that the same characteristic mass has been recovered after eliminating from the training set the direct information concerning the mass, through the galaxy luminosity. One may suspect that the compaction events are especially pronounced in galaxies near the critical mass primarily due to the fact that supernova feedback, which weakens compactions in lower masses, becomes inefficient near and above this mass (Dekel et al. 2019b). The characteristic mass for compaction events, being in the ball park of the mass threshold for discs seen in Fig. 2, may indicate that the compaction events also have a major role in the transition from non-discs to discs, to be addressed in this paper.

3.2 Post-compaction discs and rings in simulations

3.2.1 Discs and rings about a massive bulge

Fig. 4 displays the evolution of one VELA galaxy through the compaction and BN events and the post-compaction phases. It shows face-on images of projected gas density that can serve as a proxy for the associated SFR following the Kennicutt–Schmidt relation. The compaction phase (top-left panel) leads to a BN (top-middle) that is characterized by the central blob of high gas density. Immediately after (top-right), a highly turbulent rotating disc develops and grows in extent (bottom-left). It shows a pronounced spiral-arm pattern and irregular perturbations including giant clumps. This is a VDI phase, in which the giant clumps and the gas between them migrate inwards (Noguchi 1998; Bournaud et al. 2007; Dekel et al. 2009b; Ceverino et al. 2010, 2012; Bournaud et al. 2011; Ceverino et al. 2012). Then, the central gas is depleted into star formation and outflows (in comparable roles, Zolotov et al. 2015), and an extended clumpy ring forms, continuously fed by incoming cold streams, showing tightly wound spiral arms and giant clumps (bottom-middle). The ring is maintained at its extended form for several Gigayears, with no significant inward migration (bottom-right).

The complementary stellar-density maps in the lower six panels show how a compact stellar system forms following the gas compaction process into the BN phase (top-middle), and how it remains massive and compact as it quenches to a passive red nugget. The compaction process thus results in a massive central bulge, which soon becomes surrounded by a gaseous disc that develops into an extended ring. We will argue below that this massive bulge is a key for ring longevity.

Fig. 5 indicates that the ring phenomenon is robust. It shows examples of images of face-on projected gas density in several simulated post-compaction galaxies with extended gas rings, three at $z > 1$ and one at $z \sim 4$. These examples will serve as our fiducial pronounced rings in the simulations. These cases illustrate the robustness of rings about massive bulges in post-compaction galaxies, above the critical mass for major compaction events.

In order to explore the buildup of the rings through the different phases, Fig. 6 shows the evolution of surface-density radial profiles in the disc plane for (mostly cold) gas as well as SFR, stars, and metallicity. Three VELA galaxies that develop pronounced rings are shown, each at four phases of evolution corresponding to pre-compaction, compaction, early post-compaction, and late post-compaction, as seen in Fig. 4, with the corresponding redshifts marked. Inspecting the evolution of the gas profiles, one can see the

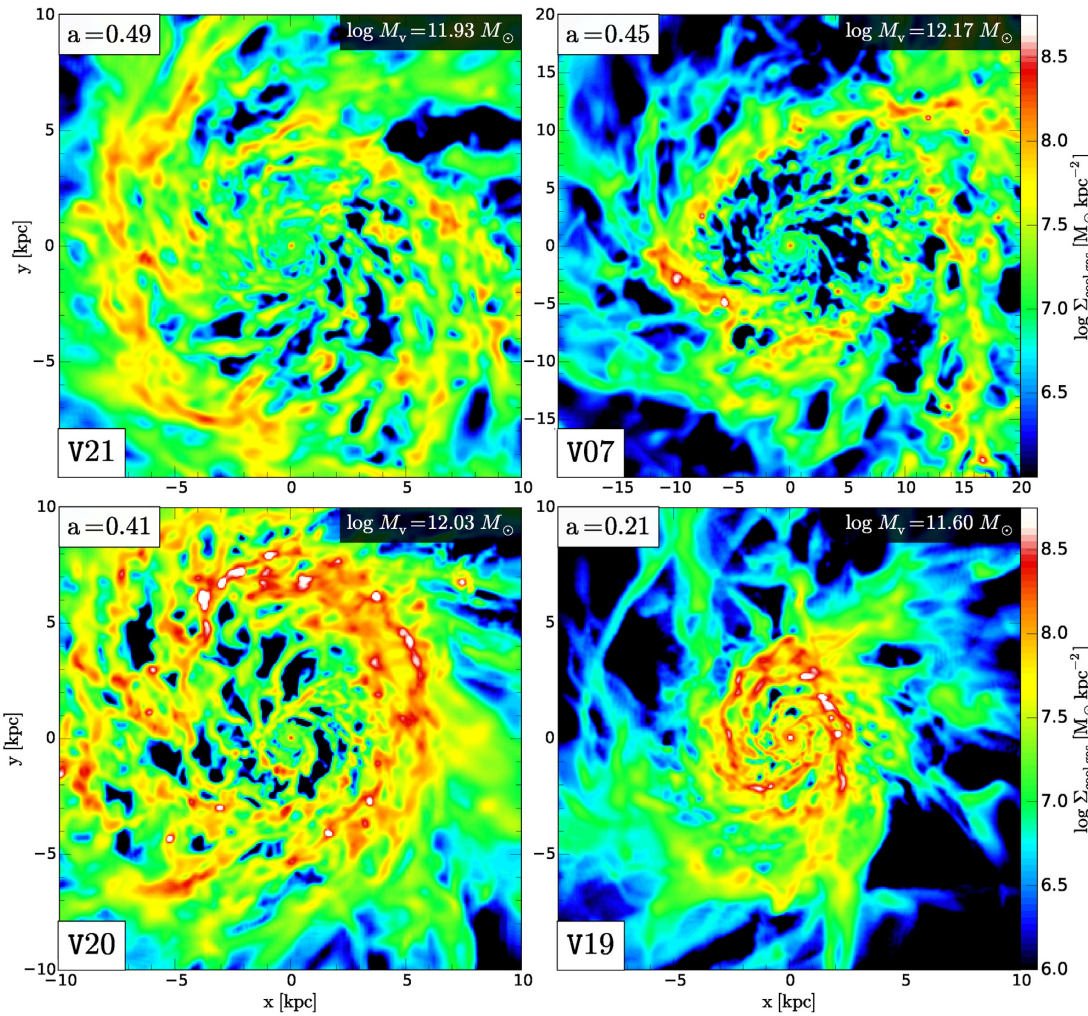


Figure 5. Post-compaction rings. Face-on projected images of gas density in four VELA galaxies at their post-compaction phase, displaying pronounced extended clumpy star-forming rings, fed by cold streams, surrounding gas-depleted central regions. The corresponding stellar density maps show massive compact central bulges.

growth of gas density inside $r \sim 1$ kpc during the compaction phase, followed by gas depletion in the inner few kpc and the development of a long-term ring at $r \sim 10$ kpc post-compaction. The SFR density profiles roughly follow the gas density profiles, obeying the KS relation, showing the ring as well.

The stellar profiles show the associated post-compaction growth of the stellar mass within the sphere encompassed by the ring, which can be translated to a decrease in the quantity δ_d of equation (2) that determines the inward mass transport rate via equation (24) below. The ring itself is hardly detectable in most stellar mass profile. The metallicity is decreasing with radius, being ~ 0.4 dex lower in the ring compared to the inner disc. This indicates that the ring is being built by freshly accreted gas.

Based on the robust occurrence of clumpy post-compaction discs and rings in the simulations, we propose that they can be identified with a large fraction of the observed massive and extended star-forming rotating and highly turbulent ‘discs’ showing giant clumps (Genzel et al. 2008, 2014; Guo et al. 2015, 2018; Förster Schreiber et al. 2018). The long-term survival of these gravitationally unstable rings, in the simulations and in the observed galaxies, seems to be in apparent conflict with the expected rapid inward migration of VDI discs discussed in Section 2.3 based on Dekel et al. (2009b), and

it thus poses a theoretical challenge which we address in Section 4 below.

3.2.2 Compaction-driven transition to rotating discs/rings

The kinematic transition through the BN event is of particular relevance to our current study of extended discs and rings. In order to see this, Fig. 7 shows the transition of kinematic properties through the BN event and, almost equivalently, through the crossing of the threshold mass, in the VELA simulations (see similarly the evolution of spin in Jiang et al. 2019, fig. G1). The galaxies evolve from pressure to rotation support, with the median V_{rot}/σ growing from near unity to about 4 ± 1 . The important fact to note is that it is the rotation velocity that is dramatically growing during the compaction process, from a small $V_{\text{rot}}/V_v = 0.4 \pm 0.1$ pre-compaction to $V_{\text{rot}}/V_v = 1.4 \pm 0.1$ post-compaction. During the same period, over which the normalizing factor V_v does not vary significantly, the velocity dispersion remains roughly constant at about $\sigma/V_v = 0.4 \pm 0.1$.

We learn that the transition from pressure to rotation support is not because of a significant change in the stirring of turbulence, but rather due to an abrupt increase in the gas AM. This indicates that the inflowing high-AM gas is prevented from forming a long-lived

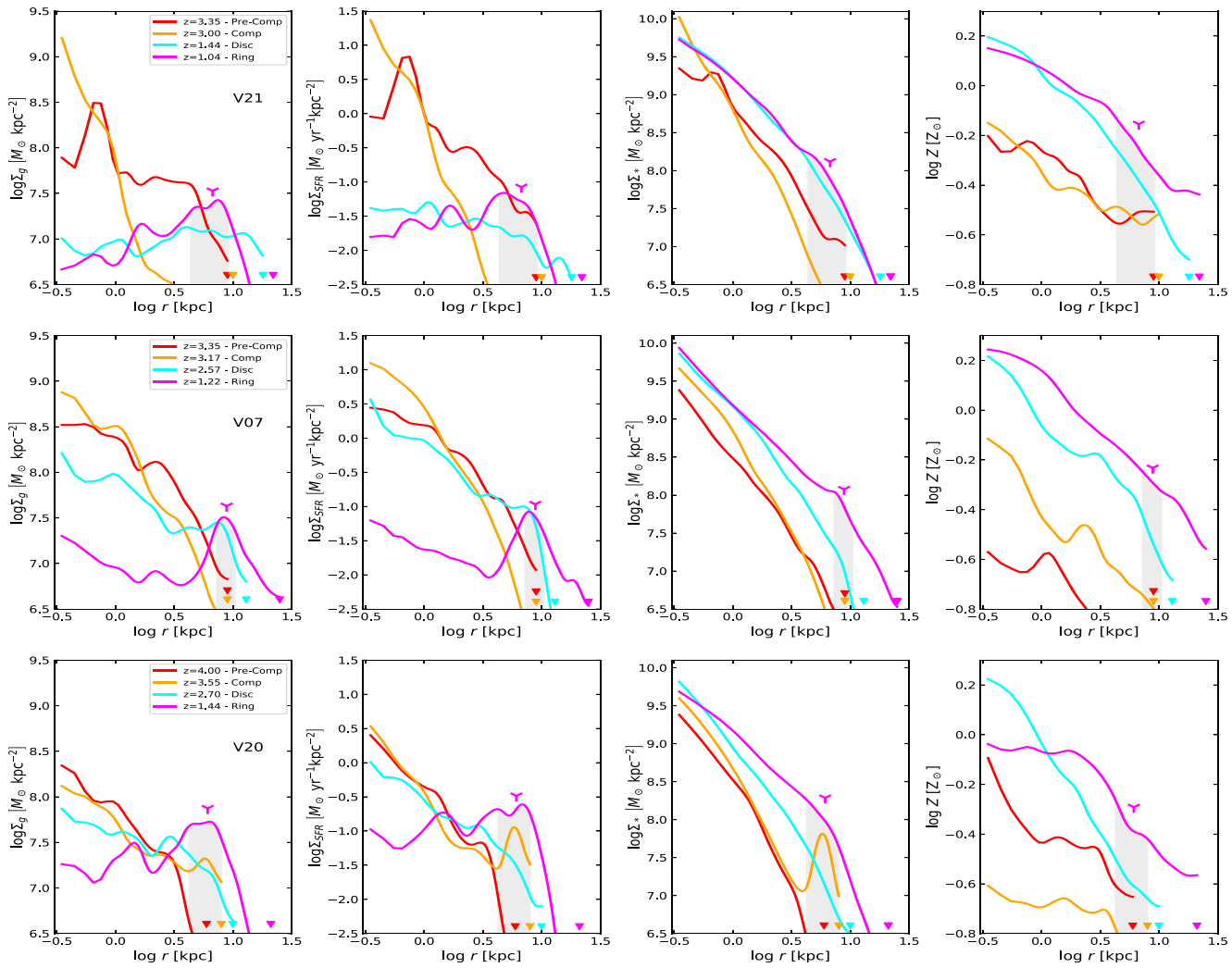


Figure 6. Evolution of profiles through compaction and ring formation. Shown are surface-density radial profiles of gas, SFR, stars, and metallicity for three of the VELA galaxies that develop pronounced rings. The profiles for each galaxy are shown at the four phases of evolution (see Fig. 4), namely pre-compaction (red), during compaction (yellow), early post-compaction (cyan), and late post-compaction (magenta), at the redshifts indicated. The profiles are smoothed with a Gaussian of standard deviation 0.05 in $\log r$. The triangles mark the disc radii R_d . The shaded area marks the $\pm 1\sigma$ ring width in gas at the late post-compaction phase, and the wedge marks r_0 . The gas and SFR profiles show the post-compaction appearance of a ring. It is associated with a growth in the stellar mass encompassed by the ring, namely within 5–10 kpc (note the different vertical axes for gas and stars). The metallicity in the ring is low, reflecting the fact that it is largely made of freshly accreted gas.

disc in the pre-compaction phase because of an efficient loss of AM, largely due to the merger-driven flips discussed in Section 2.2 based on Dekel et al. (2020). In turn, the gas seems to retain its incoming high AM in the post-compaction phase. This should guide our effort in Section 4 below to understand the post-compaction survival of extended rings by means of AM exchange.

Also shown in Fig. 7 is the measure of disciness, V_{rot}/σ , for all VELA snapshots as a function of the time with respect to the major BN event, as well as the virial mass (colour). The visual impression is that the correlation with the BN event is rather tight, showing a clear transition from non-discs to discs near the BN event, where the halo mass is near a threshold of $\sim 2 \times 10^{11} M_\odot$. In particular, there is only a small number of cases (except very massive ones) where the galaxies are non-discs significantly after the BN phase. This is yet another possible hint that the formation of a massive central bulge, in the mass range where mergers are infrequent, is in most cases sufficient for disc or ring longevity.

We thus have a hint that the simulations show a correlation between the compaction to a BN and the development of an extended gas disc or ring. In Section 3.3, we quantify the ring properties and establish this correlation explicitly for the rings, and in Section 4 we attempt to understand the origin of this correlation.

3.3 Ring properties and correlation with nuggets

3.3.1 Ring detection and properties

For crude estimates of expected ring properties, we read from the surface-density profiles of the VELA galaxies with pronounced rings (Figs 5 and 6) that the galaxies of $M_s \sim 5 \times 10^{10} M_\odot$ have mean gas surface densities in the ring of $\Sigma_{\text{gas}} \sim 5 \times 10^7 M_\odot \text{ kpc}^{-2}$, while much of the SFR occurs in clumps of $\Sigma_{\text{gas}} \sim 5 \times 10^8 M_\odot \text{ kpc}^{-2}$. In a ring of radius $r = 10 \text{ kpc}$ r_{10} and width $\Delta r/r = 0.33 \eta_{0.33}$, the total gas mass in the ring is $M_{\text{gas}} \sim 10^{10} M_\odot \eta_{0.33} r_{10}^2$. The average gas

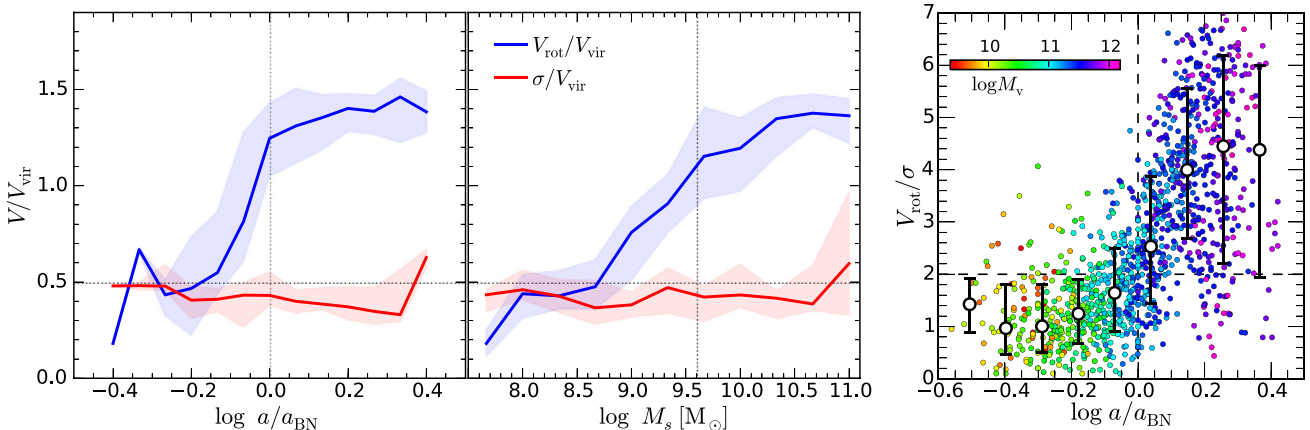


Figure 7. Kinematic evolution through compaction into rotation-supported discs/rings. Shown is the evolution of rotation velocity V_{rot} and velocity dispersion σ_r in VELA galaxies. Left: The median velocities (and 1σ scatter), with respect to the BN event (left) and, quite similarly, as a function of stellar mass M_s (right). We see that the rotation velocity is increasing drastically during the compaction and BN phase, while the velocity dispersion remains roughly constant across this event. This argues that angular momentum is a key to understanding the emergence of post-BN discs, and hints to extended rings as they naturally possess high AM. Right: The disciness measure V_{rot}/σ_r , for all VELA snapshots, as a function of time with respect to the BN event. The symbol colour marks M_v . Symbols with error bars are medians in bins of a . We see a relatively tight correlation between the transition from non-discs to discs and the compaction-driven BN event where the galaxy mass is near a threshold of $\sim 2 \times 10^{11} M_\odot$, hinting that the formation of a massive compact bulge is an important driver of disc or ring formation and longevity.

number density in the ring is $n \sim 1 \text{ cm}^{-3}$. The average SFR density in these pronounced rings is $\Sigma_{\text{sfr}} \sim \Sigma_{\text{gas}}/t_{\text{sfr}}$, which for $t_{\text{sfr}} \sim 0.5 \text{ Gyr}$ gives $\Sigma_{\text{sfr}} \sim 0.1 M_\odot \text{ yr}^{-1} \text{ kpc}^{-2}$. The total SFR in the ring is therefore $\text{SFR} \sim 20 M_\odot \text{ yr}^{-1} \eta_{0.33} r_{10}^2$.

In order to more quantitatively measure ring properties for all the simulated galaxies, we compute for each the radial gas surface-density profile $\Sigma(r)$ projected on to the disc plane defined by the instantaneous angular momentum, and fit to it a function that captures the main ring with a Gaussian shape in linear Σ versus r , as described in more detail in Appendix B (available in the Supporting Information). Three examples are shown in Fig. 8 to illustrate the profiles and fits. In the case of a single dominant ring (left and middle panels), which is ~ 80 per cent of the cases where the galaxies have rings, we fit a Gaussian on top of a constant background,

$$\Sigma(r) = \Sigma_0 + \Sigma_G \exp \left[-\frac{(r - r_0)^2}{2\sigma^2} \right], \quad (4)$$

with four free parameters.

In the case where a smoothed version of the profile indicates two well-separated rings, which occurs in ~ 20 per cent of the ringy galaxies, we fit a sum of two Gaussians with the same Σ_0 (right-hand panel). If one of the rings is at least three times as massive as the other, which happens in about half the galaxies with double rings, we choose it as the dominant ring. Otherwise, in ~ 10 per cent of the cases, we combine the two rings into one, assigning to it the average contrast and a combined radius, width and mass as specified in Appendix B (available in the Supporting Information).

The ring is characterized by its contrast with respect to the background in its interior,

$$\delta_{\text{ring}} = \frac{\Sigma_g}{\Sigma_0}, \quad (5)$$

ranging from 0 for no ring to $\delta_{\text{ring}} \rightarrow \infty$ for an ultimate ring with an empty interior.

An alternative measure of ring strength is the mass excess, the ratio between gas mass in the ring and the total in the disc including

the background,

$$\mu_{\text{ring}} = \frac{M_{\text{ring}}}{M_{\text{gas,tot}}}. \quad (6)$$

The ring mass is taken to be the mass above Σ_0 in the range $r_0 \pm 2\sigma$, and the total mass is measured from $r = 0$ to $r_0 + 2\sigma$. The mass fraction μ_{ring} thus ranges from zero for no ring to unity for a pure ring with otherwise no disc component.

In order to evaluate the quality of the two measures of ring strength, Fig. 9 plots the two against each other. For the more significant rings the two measures are tightly correlated, spread about the line $\log \mu_{\text{ring}} = \log \delta_{\text{ring}} - 0.5$, except for the very strong rings where δ_{ring} becomes $\gg 1$. The scatter is larger for the more minor rings. We note that a threshold in μ_{ring} implies a meaningful threshold in δ_{ring} . For example $\log \mu_{\text{ring}} > -1.0, -0.7, -0.5, -0.3$ automatically implies $\log \delta_{\text{ring}} > -0.7, -0.5, -0.3, 0.1$ respectively. On the other hand, a thresholds in δ_{ring} allows a large range of low μ_{ring} values. We conclude that μ_{ring} is a more robust measure of ring strength, and adopt it in our analysis below.

Fig. B1 in Appendix B (available in the Supporting Information) shows the distributions of certain ring properties among the simulated galaxies with significant rings, $\mu_{\text{ring}} > 0.3$. Other relevant properties will be discussed below in different specific contexts.

3.3.2 Compaction-driven rings

The causal connection between the compaction to a BN and the presence of a ring can now be quantified using the ring properties measured from the simulations.

Recalling that the major BNs events tend to occur at a characteristic mass in a broad redshift range, we start by exploring the typical ring strength as a function of mass and redshift. For this, Fig. 10 displays the ring mass excess, averaged within square bins in the M_v-z plane. Shown below in Fig. 13 is the associated distribution of f_{ring} , defined as the fraction of galaxies with significant rings obeying $\mu_{\text{ring}} > 0.3$. We recall from Fig. 2 (based on Dekel et al. 2020) that $M_v \sim 2 \times 10^{11} M_\odot$ is the threshold for long-lived discs, as discs in lower

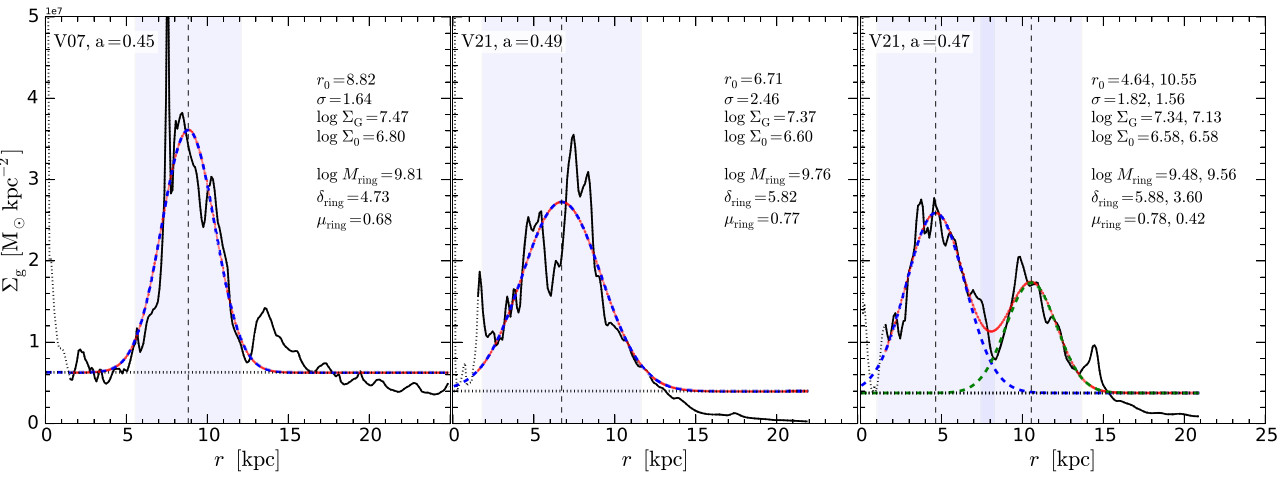


Figure 8. Measuring rings. Three examples of gas surface brightness profiles and the best-fit Gaussian fitting functions, with either one or two Gaussians above a constant background, equation (4). The four best-fit parameters are quoted for each ring. The ring is characterized by its contrast $\delta_{\text{ring}} = \Sigma_G/\Sigma_0$ and by the gas mass excess in the ring $\mu_{\text{ring}} = M_{\text{ring}}/M_{\text{gas, tot}}$, where the ring mass is measured within $r_0 \pm 2\sigma$ and the total gas is inside $r_0 + 2\sigma$. In the case of two Gaussians, if one ring is three times as massive as the other the massive one is chosen (~ 10 per cent of the ringy galaxies). Otherwise, the two rings are combined (~ 10 per cent of the ringy galaxies).

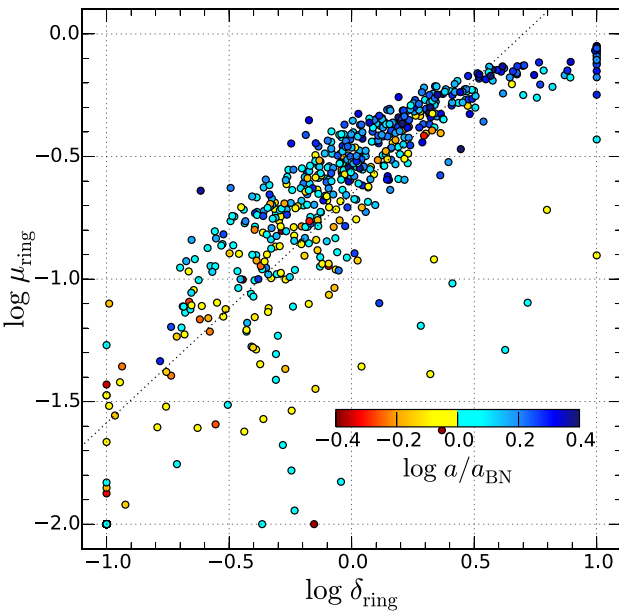


Figure 9. Ring strength. The two measures of ring strength are compared, the mass excess μ_{ring} and the density contrast δ_{ring} . For the significant rings the two measures are tightly correlated, roughly about the line $\log \mu_{\text{ring}} = \log \delta_{\text{ring}} - 0.5$. We find μ_{ring} to be more useful because a threshold in μ_{ring} implies a threshold in δ_{ring} , but not vice versa.

mass haloes are disrupted by merger-driven spin flips on time-scales shorter than the orbital times, as well as by supernova feedback. We learn that a significant fraction of the galaxies of halo masses $M_v > 10^{11.3} M_\odot$ at $z = 1\text{--}4$, where discs dominate, actually have significant rings. In this redshift range, weaker rings show up also in a fraction of the haloes somewhat below the threshold mass, where they are expected to be less long-lived. At lower masses, $M_v < 10^{10} M_\odot$, or at higher redshifts, $z > 6$, there are almost no rings. This is not surprising given that there are no long-lived discs there, as seen in Fig. 2.

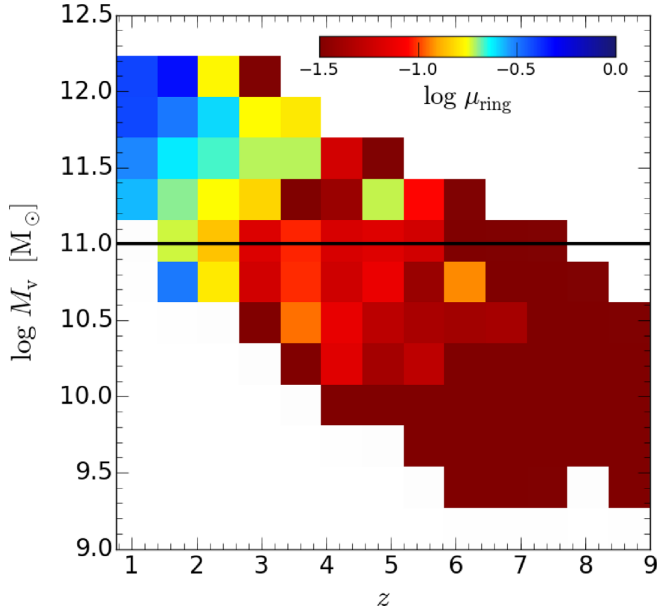


Figure 10. Ring mass excess as a function of mass and redshift. Shown is the distribution of μ_{ring} , averaged within bins in the M_v-z plane. The corresponding distribution of the fraction of galaxies with significant rings is shown in Fig. 13. We recall from Fig. 2 that long-lived discs or rings are expected to dominate above a threshold mass of $M_v \sim 2 \times 10^{11} M_\odot$ at all redshifts. We see that significant rings dominate above the threshold mass at $z < 4$, while there are weaker or no rings at much lower masses and higher redshifts. The weakness or absence of rings in intermediate-mass galaxies at very high redshifts indicates that a process other than spin flips also has a role in ring survival.

An interesting feature is the absence of rings at high redshifts near and even slightly above the threshold mass for long-lived discs, which does not follow the insensitivity to redshift seen for discs in general in Fig. 2. This indicates that the formation and survival of rings is not solely determined by the infrequent merger-driven spin flips that provides a necessary condition for long-term disc survival.

The galaxies develop long-lived outer rings only after they undergo certain stages of evolution, possibly after their major compaction events, and, as we shall see in Section 4, they should also obey another condition associated with the quantity δ_d of equation (2) that provides a sufficient condition for long-term rings.

In order to better establish the causal connection between a compaction to a BN and the development of a ring, the left-hand panel of Fig. 11 shows the ring mass excess μ_{ring} as a function of the cosmological expansion factor $a = (1 + z)^{-1}$ with respect to the BN event at a_{BN} , for all snapshots of all galaxies. Almost equivalently, the symbol colour shows these quantities as a function of stellar mass M_s . The distributions of these ring properties at given mass bins are indicated by the medians and the 25 and 75 per cent percentiles for all galaxies (black, shade). The medians are also shown for the subsample of snapshots that show rings with non-vanishing μ_{ring} values (blue). Also shown (magenta) is the fraction of galaxies that have significant rings, with $\mu_{\text{ring}} > 0.3$.

When inspecting the whole sample of simulated galaxy, we see a pronounced transition near the major compaction events to BNs at a critical mass $M_s \lesssim 10^{10} M_\odot$. Prior to the BN, the vast majority of the galaxies show no rings, while sufficiently after the BN, most of the galaxies show rings. Focusing on the galaxies with rings, we see gradual strengthening with mass, where the median mass excess is growing from $\mu_{\text{ring}} \sim 0.1$ to 0.5. Well above the critical mass, post-BN, the most pronounced rings approach $\mu_{\text{ring}} \sim 1$, namely pure rings with no gas in the interior disc. The fraction of galaxies with significant rings is rising from ~ 10 per cent pre BN and below the BN mass to ~ 65 per cent well after the BN time and above the BN mass. The exact quoted fractions are to be taken with a grain of salt as the VELA suit is not a statistically representative sample of galaxies in terms of mass function.

To further establish the correlation between rings and the post-compaction phase, the right panel of Fig. 11 displays the probability distributions of ring mass excess in three different phases of evolution with respect to the BN event. The pre-BN phase is defined here by $\log(a/a_{\text{BN}}) < -0.05$, to avoid the late compaction phase near the BN. The early-post-BN phase is limited to $0.0 < \log(a/a_{\text{BN}}) < 0.15$ and the late-post-BN phase is defined as $\log(a/a_{\text{BN}}) > 0.15$. These phases roughly correspond to different mass bins with respect to the characteristic BN mass of $M_s \sim 10^{10} M_\odot$. We read from the histograms that pre BN less than ~ 20 per cent of the galaxies show rings, all weak with a median $\mu_{\text{ring}} \sim 0.2$ for the rings. In contrast, late post-BN ~ 70 per cent of the galaxies show rings, mostly significant with a median above $\mu_{\text{ring}} \sim 0.3$. We read that ~ 24 per cent of the galaxies are expected to have pronounced rings of $\mu_{\text{ring}} > 0.5$, and ~ 50 per cent are significant rings with $\mu_{\text{ring}} > 0.3$, while ~ 30 per cent have no sign of a ring.

Fig. 12 shows the distribution of ring fraction in the M_v-z plane for significant rings of $\mu_{\text{ring}} > 0.3$. Fig. B2 in Appendix B (available in the Supporting Information) shows similar maps for all rings of $\mu_{\text{ring}} > 0.01$ and for the pronounced rings of $\mu_{\text{ring}} > 0.5$. Fig. B3 in Appendix B (available in the Supporting Information) shows the same map for significant rings $\mu_{\text{ring}} > 0.3$ but with M_v replaced by stellar mass M_s , to make the comparison with observations more straightforward. This complements the map of ring strength shown in Fig. 10. We see that a high fraction of rings is detected above the threshold mass, $M_v > 10^{11} M_\odot$, where discs survive spin flips (Fig. 2), and at $z < 4$. Focusing on massive galaxies, we read that the fraction of strong rings, $\mu_{\text{ring}} > 0.5$, is ~ 30 per cent at $z \sim 1$, while it drops to the ~ 10 per cent level at $z = 1.5-3.5$. The fraction of significant rings is ~ 50 per cent at $z \sim 1$ and $30-40$ per cent at $z = 2-4$. The fraction of all rings, including marginal minor ones, is ~ 70 per cent

at $z = 1-3$, $\sim 50-60$ per cent at $z = 3-4$ and $\sim 20-40$ per cent at $z = 4-6$. In comparison, according to Fig. 10, the average ring strength in massive galaxies is just below $\mu_{\text{ring}} = 0.5$ at $z \sim 1$, and is $\mu_{\text{ring}} = 0.3$ at $z = 1.5-4$. These fractions and ring strengths are to be compared to observations, where preliminary indications for qualitative agreement are discussed in Section 6.2.2.

The correlation of ring strength and time or mass with respect to the BN phase, as seen in Figs 10–12, strengthens our earlier impression that ring formation is correlated with the post-compaction phase of evolution, which was based on visual inspection of rings in gas images and profiles in the different evolution phases (Figs 4–6), combined with the post-compaction appearance of discs (or rings) above the corresponding mass thresholds (Figs 2 and 7). We next attempt to understand the origin of the post-compaction longevity of the rings.

4 RING STABILIZATION BY A CENTRAL MASS: AN ANALYTIC MODEL

Having established in the simulations the ring formation and survival after compaction to a massive central body, and given the conflicting expectation for a rapid inward transport in a gaseous VDI disc summarized in Section 2.3, we now proceed to an analysis that reveals the conditions for slow inward mass transport of an extended ring (Section 4.1). Then, combined with the conditions for faster ring buildup by high-AM accretion and faster interior depletion by star formation, we obtain the condition for ring formation and longevity (Section 4.2). The longer lifetime of high-contrast rings is discussed (Section 4.3), as well as the ring instability to clump formation (Section 4.4). Finally, we test certain aspects of the model using the simulations (Section 4.5).

4.1 Transport in by torques from spiral structure

4.1.1 The torque

In order to estimate the rate of inward transport of ring material [through AM conservation, or the angular Euler equation (equation 6.34 of Binney & Tremaine 2008, hereafter BT)], we wish to compute the relative AM change in the outer disc outside radius r due to torques exerted by the perturbed disc inside r , during one disc orbital time. For an order-of-magnitude estimate, we follow Chapter 6 of BT assuming a tightly wound spiral-arm pattern in a razor-thin disc. The z -component of the torque per unit mass at a position (r, ϕ) in the disc plane is

$$\tau(r, \phi) = -\frac{\partial \Phi}{\partial \phi}, \quad (7)$$

where Φ is the gravitational potential, and r and ϕ are the usual spherical coordinates. The relevant part of the potential exerting the torque is due to the disc, Φ_d , which is related to the density in the disc ρ_d via the Poisson equation. The total torque on the ring outside r is obtained by an integral over the volume outside r ,

$$T(r) = \int_r^\infty dV \rho_d \tau. \quad (8)$$

This is a simplified version of the more explicit expression in equation 6.14 of BT. After some algebra, the general result is

$$T(r) = \frac{r}{4\pi G} \int_0^{2\pi} d\phi \frac{\partial \Phi_d}{\partial r} \frac{\partial \Phi_d}{\partial \phi} |_r. \quad (9)$$

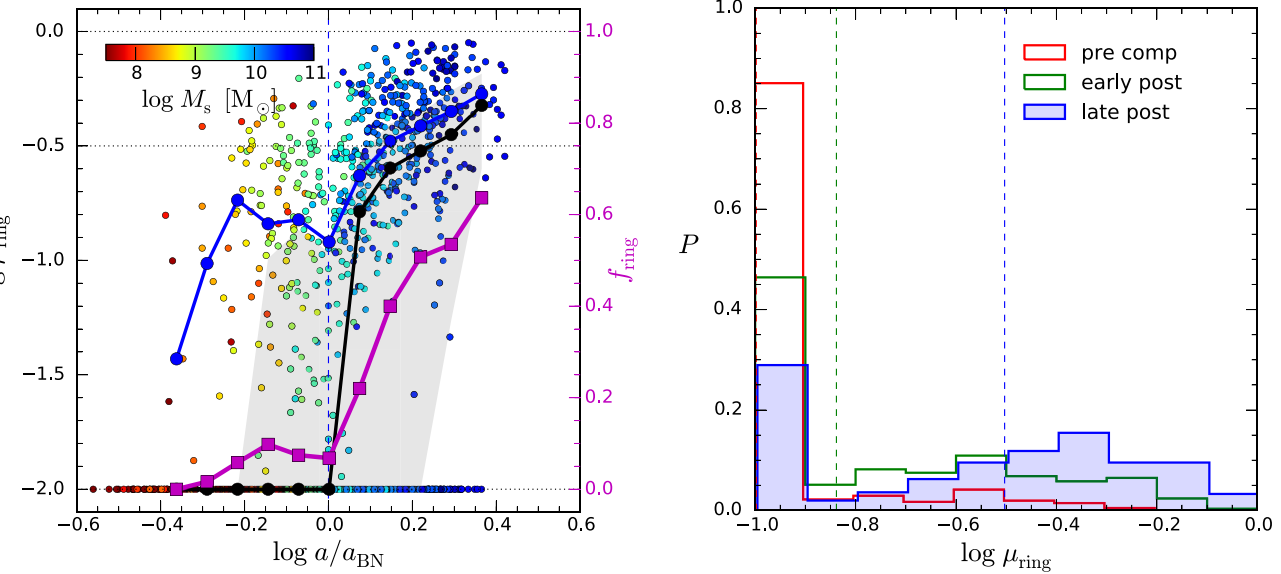


Figure 11. Ring strength and the BN event. Left: Ring mass excess μ_{ring} as a function of expansion factor $a = (1 + z)^{-1}$ with respect to the BN time a/a_{BN} for all simulated galaxies. Symbol colour marks stellar mass, which is strongly correlated with a/a_{BN} . Symbols where $\mu_{\text{ring}} < 0.01$ are put at 0.01. The medians at given mass bins for all simulated galaxies are shown in black with the 25 and 75 per cent percentiles marked by the shaded area. The medians limited to the galaxies that show rings are marked in blue. The magenta curve and the right axes refer to the fraction of galaxies with significant rings of $\mu_{\text{ring}} > 0.3$. We see a pronounced transition near the major compaction events to blue nuggets at $M_s \sim 10^{10} M_\odot$, from a tendency to have no rings to a dominance of high-contrast, massive rings. The ring excess is gradually growing with galaxy mass and time with respect to the BN phase. Right: The distribution of gas ring mass excess μ_{ring} in three different stages of evolution with respect to the BN event, roughly corresponding to different mass bins with respect to $M_s \sim 10^{10} M_\odot$. Pre BN (black), early post-BN (blue) and late post-BN (red) refer to $\log(a/a_{\text{BN}})$ prior to -0.05 , between 0.00 and 0.15 , and after 0.15 , respectively. The medians are marked by vertical dashed lines. Pre BN only a small fraction of the galaxies show rings, all weak, while late post-BN most of the galaxies show rings, mostly significant ones.

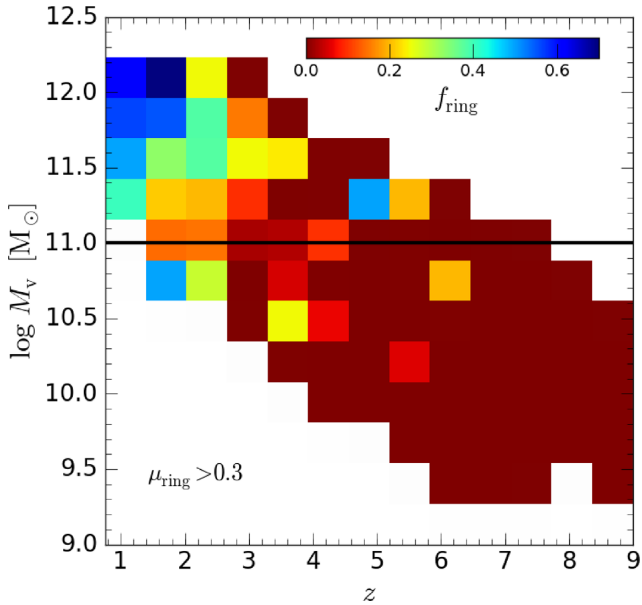


Figure 12. Fraction of significant rings. Shown is the 2D distribution of the fraction of rings with $\mu_{\text{ring}} > 0.3$ in the M_v-z plane. Similar maps for all rings with $\mu_{\text{ring}} > 0.01$ and for pronounced rings with $\mu_{\text{ring}} > 0.5$ are shown in Fig. B2 in Appendix B (available in the Supporting Information). This complements the distribution of ring strength in Fig. 10. We see that a high fraction of rings is detected above the threshold mass, $M_v > 10^{11} M_\odot$, where discs survive spin flips (Fig. 2), and at $z < 4$.

Next, assuming a tightly wound spiral structure with m arms, the small pitch angle is given by

$$\tan \alpha = \frac{m}{|k|r} \ll 1, \quad (10)$$

with k the wavenumber (positive or negative for trailing or leading arms respectively). One assumes a thin disc, in which the spiral structure is described by a surface density (equation 6.19 of BT):

$$\Sigma(r, \phi) = \Sigma_1(r) \cos[m\phi + f(r)], \quad (11)$$

where $\Sigma_1(r)$ is the spiral perturbation, assumed to vary slowly with r , the shape function is $f(r)$ where $df/dr = k$, the spirals are tightly wound $|k|r \gg 1$, and $m > 0$. The corresponding potential is

$$\Phi_d = \Phi_1(r) \cos[m\phi + f(r)], \quad \Phi_1 = -\frac{2\pi G \Sigma_1}{|k|}. \quad (12)$$

The torque is then (equation 6.21 of BT)

$$T(r) = \text{sgn}(k) \frac{mr \Phi_1^2}{4G} = \text{sgn}(k) \frac{\pi^2 m r G \Sigma_1^2}{k^2}. \quad (13)$$

Thus, trailing arms ($k > 0$) exert a positive torque on the outer part of the disc and therefore transport AM outwards (we omit the sign of the torque hereafter). Using equation (10), the torque becomes

$$T(r) = \frac{\pi^2 G r^3}{m} \Sigma_1^2 \tan^2 \alpha. \quad (14)$$

We should comment that spiral arms are indeed usually trailing. Across the trailing spiral, the gas rotates faster than the spiral pattern (section 6.1.3.d of BT), namely the ring in this region is well inside the co-rotation radius of the spiral. The pattern speed for the spiral pattern may be not unique, at different radii or at different times,

because of the varying potential due to the growth of the bulge. Nevertheless, the torque from the trailing spirals is transferring AM from inside to outside the co-rotation radius and consequently gas in the ring flows inwards. We discuss these issues further in the context of rings at resonance radii in Section 7.1.

4.1.2 Angular-momentum transport and mass inflow rate

In order to compute the relative change of AM in the ring during an orbital time, we write for a ring at radius r the torque per unit mass as $\tau(r) = T(r)/M_r$, where M_r is the ring gas mass,

$$M_r = 2\pi r^2 \eta_r \Sigma_r, \quad (15)$$

and where Σ_r is the average surface density in the ring and $\eta_r = \Delta r/r$ is the relative width of the ring. The specific AM in the ring is $j = \Omega r^2$, and the orbital time is $t_{\text{orb}} = 2\pi/\Omega^{-1}$, where Ω is the circular angular velocity at r . Substituting in equation (14), the relative change of AM during one orbit is

$$\frac{\Delta j}{j} \Big|_{\text{orb}} = \frac{\tau t_{\text{orb}}}{j} = \frac{\pi^2 G}{m \Omega^2 r \Delta_r \eta_r} A_m^2 \Sigma_d \tan^2 \alpha, \quad (16)$$

where $\Delta_r = \Sigma_r/\Sigma_d$ is the ring contrast with respect to the disc,² which we first assume to be $\gtrsim 1$, and where the amplitude of the spiral surface-density pattern is assumed to be a fraction A_m of the axisymmetric density,

$$\Sigma_1(r) = A_m \Sigma(r). \quad (17)$$

For reference, this amplitude is known to be in the range 0.15–0.60 in observed spiral galaxies.

It turns out that the quantity that governs the relative AM change and simplifies the above expressions for a ring is the same mass ratio of cold disc to total that governs the rapid inflow of a VDI disc, equation (2), namely $\delta_d = M_d/M_{\text{tot}}$, where M_d is the cold mass in the disc. Using equations (2) and (15), and approximating the circular velocity by $(\Omega r)^2 = GM_{\text{tot}}(r)/r$, the surface density in the disc can be expressed in terms of δ_d ,

$$\Sigma_d = \frac{M_d}{\pi r^2} = \frac{\Omega^2 r}{\pi G} \delta_d. \quad (18)$$

Inserting this into equation (16) we obtain

$$\frac{\Delta j}{j} \Big|_{\text{orb}} = \frac{\pi}{m \Delta_r \eta_r} A_m^2 \delta_d \tan^2 \alpha. \quad (19)$$

Next, the pitch angle can also be related to the key variable δ_d by appealing to the local axisymmetric Toomre instability, which yields a critical wavenumber for the fastest growing mode of instability (equation 6.65 of BT),

$$k_{\text{crit}} = \frac{\kappa^2}{2\pi G \Sigma} = \frac{\psi^2}{2r} \delta_d^{-1}. \quad (20)$$

Here κ is the epicycle frequency, $\kappa^2 = r d\Omega^2/dr + 4\Omega^2$. This gives $\kappa = \psi \Omega$, where $\psi = 1$ for Keplerian orbits about a point mass, $\psi = \sqrt{2}$ for a flat rotation curve, $\psi = \sqrt{3}$ for the circular velocity of a self-gravitating uniform disc, and $\psi = 2$ for a solid-body rotation. The second equality made use of equation (18). Adopting $|k| = k_{\text{crit}}$ in equation (10) for the pitch angle, we obtain

$$\tan \alpha = \frac{2m}{\psi^2} \delta_d. \quad (21)$$

²This is related to δ_{ring} of equation (5) and Fig. 9 simply by $\Delta_r = 1 + \delta_{\text{ring}}$.

Inserting this in equation (19) we get

$$\frac{\Delta j}{j} \Big|_{\text{orb}} = \frac{4\pi m}{\psi^4 \Delta_r \eta_r} A_m^2 \delta_d^3. \quad (22)$$

The rate at which AM is transported out is actually driven by the sum of the gravitational torques computed above and the advective current of AM. The advective transport rate is given by the same expression as in equation (13) times a factor of order unity or smaller, explicitly $[v_s^2 |k|/(\pi G \Sigma) - 1]$, where v_s is the speed of sound (BT, equation 6.81, based on appendix J). Thus, the advective transport is generally comparable in magnitude to or smaller than the transport by gravitational torques. We therefore crudely multiply the AM exchange rate of equation (22) by a factor of two.

The inverse of Δ/j in an orbital time is the desired time-scale for the ring mass to be transported inwards with respect to the orbital time,

$$t_{\text{inf}} \sim \frac{\psi^4}{8\pi m} \frac{\Delta_r \eta_r}{A_m^2} \delta_d^{-3} t_{\text{orb}}. \quad (23)$$

With the fiducial values $\psi = \sqrt{2}$, $m = 2$, $\Delta_r = 1$, $A_m = 0.5$, and $\eta_r = 0.5$ we finally obtain

$$t_{\text{inf}} \sim 5.89 \delta_{d,0.3}^{-3} t_{\text{orb}}. \quad (24)$$

We learn that, for a fixed value of η_r that does not strongly depend on δ_d , the inward mass transport rate is very sensitive to the value of δ_d . A value near unity implies a rapid inflow, while for $\delta_d \ll 1$ the inflow rate is very slow.

With $\delta_d \lesssim 1$, e.g. corresponding to a bulge-less very gas-rich disc in radii where it dominates over the DM, equation (24) indicates a significant AM loss corresponding to inward mass transport in a few orbital times, as estimated in Dekel et al. (2009b) for a VDI disc, equation (1) above. In this case, the pitch angle is not necessarily very small, and the spiral pattern can cover a large fraction of the disc with a significant radial component. In contrast, with $\delta_d \ll 1$, equation (21) indicates that the pitch angle is very small, making the above calculation valid and practically confining the spiral arms to a long-lived ring, with a negligible mass transport rate.

A low value of δ_d is expected when M_{tot} is dominated either by a central massive bulge and/or by a large DM mass within the ring radius. The former is inevitable after a compaction event. The latter is likely when the DM halo is cuspy and when the incoming streams enter with a large impact parameter and therefore form an extended ring that encompasses a large DM mass, as may be expected at late times. A small δ_d is also expected when the gas fraction in the accretion is low, as expected at late times.

4.2 The conditions for long-lived rings

The formation and fate of the disc and the ring is determined by the interplay between three time-scales. First, an extended ring originates from high-AM spiralling-in cold streams (Section 2), which accrete mass on a time-scale t_{acc} . Second, the ring gas is transported inwards towards filling up the interior disc by torques from the perturbed disc on a time-scale t_{inf} , computed in Section 4.1. Third, this disc gas is depleted into stars and outflows on a time-scale t_{sfr} . We consider the two conditions for ring formation and longevity to be

$$t_{\text{acc}} < t_{\text{inf}} \quad \text{and} \quad t_{\text{sfr}} < t_{\text{inf}}. \quad (25)$$

When either of these conditions is violated, the ring does not survive. When $t_{\text{acc}} > t_{\text{inf}}$, the ring is evacuated into the disc before it is replenished, and when $t_{\text{sfr}} > t_{\text{inf}}$, the disc remains gaseous, both leading to a gas disc. These conditions for a disc are expected to

be fulfilled for high values of δ_d . On the other hand, a ring would form and survive if $t_{\text{acc}} < t_{\text{inf}}$, namely the ring is replenished before it is transported in, and if $t_{\text{sfr}} < t_{\text{inf}}$, causing the interior disc to be depleted of gas. These conditions for a ring are expected to be valid for low values of δ_d . We next quantify these conditions, assuming for simplicity an EdS cosmology, approximately valid at $z > 1$.

The orbital time of the extended ring is on average a few per cent of the Hubble time t_{hub} for all galaxy masses (e.g. following Dekel et al. 2013),

$$t_{\text{orb}} \sim 0.088 \lambda_{0.1} t_{\text{hub}} \sim 1.5 \text{ Gyr} (1+z)^{-3/2}. \quad (26)$$

Here $\lambda = R_{\text{ring}}/R_v$ is the contraction factor from the virial radius to the extended gas ring, here in units of 0.1, which we adopt as our fiducial value.

The accretion time-scale, the inverse of the specific accretion rate, is on average (Dekel et al. 2013)

$$t_{\text{acc}} \sim 30 \text{ Gyr} (1+z)^{-5/2} \sim 20 t_{\text{orb}} (1+z)^{-1}, \quad (27)$$

with a negligible mass dependence across the range of massive galaxies. The second equality is based on equation (26). Comparing equation (27) and equation (24) for the transport time, we obtain net *ring replenishment*, $t_{\text{acc}} < t_{\text{inf}}$, for

$$\delta_d < 0.20 (1+z)^{1/3}. \quad (28)$$

The redshift dependence is weak, e.g. $\delta_c < 0.29$ at $z = 2$.

For the depletion time, it is common to assume that the gas turns into stars on a time-scale

$$t_{\text{sfr}} \sim \epsilon_{\text{ff}}^{-1} t_{\text{ff}} \sim 5 t_{\text{orb}}, \quad (29)$$

where ϵ_{ff} is the efficiency of SFR in a free-fall time and t_{ff} is the free-fall time in the star-forming regions (e.g. Krumholz, Dekel & McKee 2012). We adopted above the observed standard value of $\epsilon_{\text{ff}} \sim 0.01$ (e.g. Krumholz 2017), and $t_{\text{ff}} \sim 0.3 t_{\text{dyn}} \sim 0.05 t_{\text{orb}}$. The latter is assuming that stars form in clumps that are denser than the mean density of baryons in the ring by a factor of ~ 10 (Ceverino et al. 2012).³ Comparing equations (29) and (24), we obtain net inner *disc depletion*, $t_{\text{sfr}} < t_{\text{inf}}$, for

$$\delta_d < 0.32. \quad (30)$$

From equations (28) and (30) we learn that the two conditions are in the same ball park, though at $z < 3$ the ring replenishment condition is somewhat more demanding, while at higher redshifts the disc depletion condition is a little more demanding. We conclude that ring formation and survival is crudely expected below $\delta_d \sim 0.2$, give or take a factor ~ 2 due to uncertainties in the values of the fiducial parameters.

We note that since the ring is primarily a gaseous phenomenon, the ring would not form and survive once the gas fraction in the disc and ring is too low. This implies a lower bound for δ_d in long-lived ring galaxies, when its low value is driven by a low gas fraction. This lower bound is estimated using the simulations to be $\delta_d \sim 0.03$ (Section 4.5).

As the ring develops, once δ_d becomes smaller than the threshold, the ring becomes overdense with respect to the disc, $\Delta_r > 1$. Then in equation (24) the inflow time-scale becomes longer accordingly so the ring can continue to grow in a runaway process.

³A similar time-scale for SFR is obtained in the VELA simulations. Using Table A1 in Appendix A (available in the Supporting Information), the ratio of gas mass to SFR at $z = 2$ is typically $t_{\text{sfr}} \sim 1 \text{ Gyr}$. With $t_{\text{orb}} \sim 0.29 \text{ Gyr}$ at that redshift from equation (26), the SFR time-scale is consistent with equation (29).

4.3 Long-lived high-contrast rings

The estimate of t_{inf} in Section 4.1.2 was valid for the stage of transition from disc to ring, namely where the disc is still gas rich with a spiral structure that exerts torques on the outer ring, namely when the ring contrast Δ_r is not much larger than unity. Once the ring develops and is long lived, under $\delta_d \ll 1$, it can become dominant over the disc. To evaluate the inflow rate in this situation, we now consider the limiting case of a pure ring, in which the spiral structure exerts torques on other parts of the ring. M_d of the previous analysis is now replaced by M_r , Σ_d in equation (18) is replaced by $\Sigma_r = (2\eta_r)^{-1} \Sigma_d$, while Δ_r is unity. Now $\Delta j/j$ in equation (19) and $\tan \alpha$ in equation (21) are both divided by $2\eta_r$, so $\Delta j/j$ in equation (22) is divided by $(2\eta_r)^3$. For otherwise the fiducial values of the parameters, and in particular for the value of η_r fixed at 0.5, the inflow time-scale is the same as it was in equation (24).

However, in the case of a tightly wound strong ring, one may relate the relative ring width to the pitch angle, assuming that the width is the ‘wavelength’ of the spiral arm, namely the radial distance between the parts of the arm separated by 2π ,

$$\eta_r = \frac{\Delta r}{r} = \frac{2\pi/k}{r} = \frac{2\pi}{m} \tan \alpha = \frac{2\pi}{\psi^2 \eta_r} \delta_d, \quad (31)$$

where we used equations (10) and (21). Solving for η_r we obtain

$$\eta_r = \frac{(2\pi)^{1/2}}{\psi} \delta_d^{1/2}. \quad (32)$$

Then from equation (22) divided by $(2\eta_r)^3$ we obtain

$$\frac{\Delta j}{j|_{\text{orb}}} = \frac{m}{8\pi} A_m^2 \delta_d. \quad (33)$$

After multiplying by two for the advective contribution, the inflow time-scale becomes

$$t_{\text{inf}} = \frac{4\pi}{m A_m^2} \delta_d^{-1} t_{\text{orb}} = 84 \delta_{d,0.3}^{-1} t_{\text{orb}}, \quad (34)$$

where the fiducial values of $m = 2$ and $A_m = 0.5$ were assumed. This is well longer than the Hubble time and the accretion and depletion time-scales, implying that once a high-contrast ring forms, it is expected to live for long.

4.4 Ring Toomre instability to clump formation

The rings in the simulations, as seen in Fig. 5, are clumpy and star forming, as observed (e.g. Genzel et al. 2014), with the clump properties analysed in Mandelker et al. (2014, 2017). This indicates that the rings are gravitationally unstable. Can this be consistent with the rings being stable against inward mass transport?

The Toomre Q parameter can also be expressed in terms of the cold-to-total mass ratio δ_d (Dekel et al. 2009b). For a high-contrast ring at r , with a relative width η_r , mean cold surface density Σ_r , and cold mass $M_r = 2\eta_r \pi r^2 \Sigma_r$, we obtain with $V^2 = G M_{\text{tot}}(r)/r$

$$Q = \frac{\kappa \sigma}{\pi G \Sigma_r} = 2\eta_r \psi \delta_d^{-1} \left(\frac{\sigma}{V} \right), \quad (35)$$

where $\psi \sim 1-2$ (mentioned in the context of equation 20). Here δ_d refers in practice to the cold mass in the ring versus the total mass encompassed by the ring. With $\psi \sim \sqrt{2}$ and $\eta_r \sim 0.5$, this implies that a ring with $\sigma/V \sim 0.2$ (Fig. 7) could be Toomre unstable with $Q \sim 1$ if $\delta_d \sim 0.2$. This is indeed in the regime of long-lived rings based on equations (28) and (30), and certainly so in the high-contrast-rings case, equation (34). Based on Figs 13 and 14, a significant fraction of the rings have $\delta_d \sim 0.2$, especially at $z \sim 2-5$.

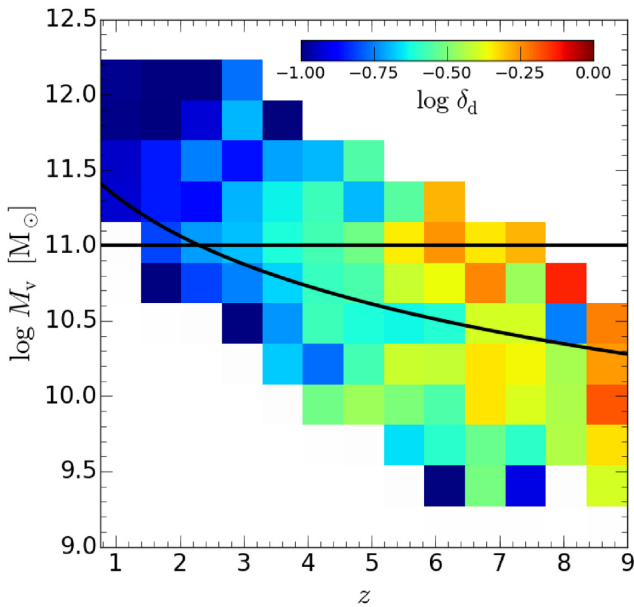


Figure 13. Analytic model versus simulations in the M_v – z plane. Shown is the average $\delta_d = M_d/M_{\text{tot}}$ in bins within the plane. This quantity is expected to govern the inward mass transport rate and thus tell where rings are expected in this plane, to be compared to the ring fraction map in Fig. 12. We see that a high fraction of rings is detected above the threshold mass, $M_v > 10^{11} M_\odot$, where discs survive spin flips (Fig. 2), and at $z < 4$. This regime is indeed where on average $\delta_d < 0.3$, as predicted in equations (28) and (30). The redshift dependence of δ_d , also reflected in the ring fraction in Fig. 12, is largely due to the general increase of gas fraction with redshift. Below the threshold mass δ_d is not too meaningful because the galaxies are dominated by non-discs (Fig. 2). The low values of δ_d at low masses could be due to gas removal by supernova feedback below the critical potential well of $V_v \sim 100 \text{ km s}^{-1}$ (black curve, Dekel & Silk 1986), but they do not lead to long-term rings because of spin flips.

In fact, it has been shown using the simulations that clumps may form even with $Q \sim 2$ –3 as a result of an excess of compressive modes of turbulence due to compressive tides during mergers or flybys (Inoue et al. 2016). This would allow clumpy rings even when $\delta_d \lesssim 0.1$. The ring could thus fragment to giant clumps and form stars while it is deep in the regime where it is stable against inward mass transport, provided that it is above the threshold for a gaseous ring, $\delta_d \sim 0.03$ (Section 4.5).

At the same time, the value of the Q parameter in the disc region encompassed by the ring can be much higher than unity, leading to ‘morphological quenching’ (Martig et al. 2009). This is because δ_d in this region is low, partly due to the high central mass and partly due to the low density of gas, which has been depleted into stars and outflows.

4.5 Model versus simulations via the cold fraction

We turn to the simulations again, now for the variable $\delta_d = M_d/M_{\text{tot}}$ that is predicted to control the ring formation and longevity according to the analytic model derived in the previous subsections. First, Fig. 13 shows in bins within the M_v – z plane the averaged values of δ_d for all galaxies. The cold mass M_d is computed in the disc within R_d including the gas and young stars, with the latter typically contributing about 20–25 per cent of the cold mass. It is divided by the total mass including gas, stars and DM in the sphere interior to the ring radius r_0 . In the absence of a ring, the total mass is computed

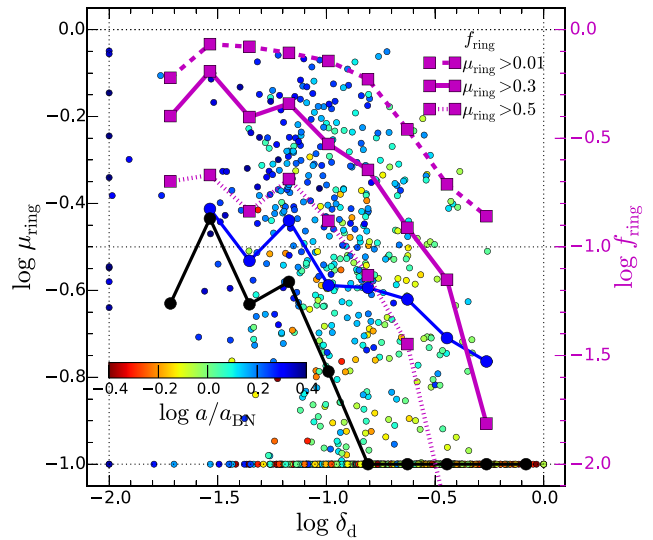


Figure 14. Analytic model versus simulations – ring strength and fraction. Shown for each galaxy is the ring gas mass excess μ_{ring} versus δ_d , the cold-to-total mass ratio interior to the ring, predicted to control the ring inward mass transport. The medians of μ_{ring} in bins of δ_d are shown for all galaxies (black, shade) and for the galaxies with rings (blue). Symbol colour marks time with respect to the BN event (correlated with mass with respect to the characteristic BN mass). Also shown is the fraction of galaxies with rings of $\mu_{\text{ring}} > 0.01$, 0.3, 0.5 (dashed, solid, dotted lines respectively) in bins of δ_d (magenta, right axis and label). We see an anticorrelation between ring strength and δ_d as predicted by the analytic model. The fraction of rings with $\mu_{\text{ring}} > 0.3$ ranges from ~ 64 per cent at $\delta_d \sim 0.03$ to ~ 9 per cent at $\delta_d \sim 0.5$. A fraction of 50 per cent in all rings is obtained near $\delta_d \sim 0.2$, in general agreement with the model prediction, equations (28) and (30). The fraction of strong rings with $\mu_{\text{ring}} > 0.5$ is ~ 20 per cent, obtained for $\delta_d \leq 0.1$, and ~ 10 per cent at $\delta_d \simeq 0.15$. The δ_d dependence of the ring fraction is expected to be similar to that of t_{inf} , and, indeed, the inverse linear relation $t_{\text{inf}} \propto \delta_d^{-1}$ of equation (34), predicted for significant rings, is roughly reproduced overall. The slight steepening of f_{ring} at higher δ_d , and the absence of rings at $\delta_d > 0.5$, are consistent with the prediction for weaker rings in equation (24). The flattening of f_{ring} at low δ_d is consistent with saturation of the ring population when t_{inf} is very long compared to all other time-scales.

within the median ring radius in the galaxies with rings, $r_0 \simeq 0.5 R_d$ (Fig. B1 in Appendix B, available in the Supporting Information).

This map of δ_d is to be compared to the maps of f_{ring} in Fig. 12 for rings of different strengths, and to the distribution of ring strength in Fig. 10. We learned there that a high fraction of rings is detected above the galaxy threshold mass, $M_v > 10^{11} M_\odot$, where discs or rings survive merger-driven spin flips according to Fig. 2 and Dekel et al. (2020), and typically at $z < 4$. This ring-dominated range in the M_v – z diagram is indeed where on average $\delta_d < 0.3$, consistent with the analytic predictions in equations (28) and (30). These low values of δ_d are largely due to the post-compaction massive bulges that appear above a similar threshold mass.

Near the threshold mass we see an increase of δ_d with redshift roughly as $\delta_d \propto (1+z)$. This mostly reflects the general increase of gas fraction with redshift. We learn from equations (24) and (27) that the quantity that characterizes a pronounced ring is expected to depend on redshift as $t_{\text{inf}}/t_{\text{acc}} \sim 0.3(1+z)\delta_{d,0.3}^{-3}$, so it is predicted to decrease with redshift as $\propto (1+z)^{-2}$. This explains the absence of rings at high redshifts even above the mass threshold for discs, as seen in the distribution of f_{ring} .

Well below the threshold mass δ_d is not too meaningful for ring survival because these galaxies are dominated by irregular non-disc

gas configurations (Fig. 2), as discs/rings are frequently disrupted by merger-driven spin flips (Dekel et al. 2020, fig. 4). The relatively low values of $\delta_d \sim 0.1\text{--}0.2$ at low masses and moderate redshifts partly reflect little gas, possibly due to gas removal by supernova feedback. Indeed, the upper limit for effective supernova feedback at $V_v \sim 100 \text{ km s}^{-1}$ (Dekel & Silk 1986), marked in the figure by a black curve, roughly matches the upper limit for the region of low δ_d values, with a similar redshift dependence of M_v . Another contribution for the low δ_d values in this regime may come from the pre-compaction central dominance of DM (Tomasetti et al. 2016). However, these low values of δ_d do not lead to long-lived rings because they are disrupted by merger-driven spin flips (Fig. 2).

To further explore the match of the analytic model with the simulations, Fig. 14 shows more explicitly the relation between the ring strength and the variable δ_d that governs the model. Shown for each galaxy is the ring gas mass excess μ_{ring} versus δ_d , as well as the median values of μ_{ring} in bins of δ_d , for all galaxies (black, shade) and limited to the galaxies with rings (blue). Most interesting are the fractions of galaxies with rings of $\mu_{\text{ring}} > 0.01, 0.3$ or 0.5 , shown in bins of δ_d (magenta symbols and lines, as labelled, right axis). We see an anticorrelation between ring strength and δ_d as predicted by the analytic model. The fraction of rings with $\mu_{\text{ring}} > 0.3$ ranges from ~ 64 per cent at $\delta_d \sim 0.03$ to ~ 9 per cent at $\delta_d \sim 0.5$. It is encouraging to note that for all rings ($\mu_{\text{ring}} > 0.01$) the fraction is $f_{\text{ring}} = 0.5$ near $\delta_d \sim 0.2$, in general agreement with the model prediction in equations (28) and (30). We see that the fraction of strong rings with $\mu_{\text{ring}} > 0.5$ is ~ 20 per cent, obtained for $\delta_d \leq 0.1$. This fraction is ~ 10 per cent at $\delta_d \simeq 0.15$. We see an indication for a decrease in ring fraction for $\delta_d < 0.03$, as expected for galaxies with a very low gas fraction (Section 4.2).

The way f_{ring} depends on δ_d may be expected to crudely resemble that of t_{inf} . Indeed, the inverse linear relation $t_{\text{inf}} \propto \delta_d^{-1}$ predicted in equation (34) for strong rings is crudely reproduced overall. The steepening at higher values of δ_d , and in particular the absence of rings at $\delta_d > 0.5$, are consistent with the prediction in equation (24) for rings in their earlier growth phase. The flattening of the ring fraction at very low δ_d values is consistent with saturation of the ring population when t_{inf} is very long compared to the Hubble time and all other time-scales.

Another way to test the validity of the analytic model is via the ring width. Fig. 15 shows the relative ring width $\eta_r = \Delta r/r$ versus δ_d for all simulated galaxies. The width is deduced from the Gaussian fit, $\eta_r = 2\sigma/r_0$. Also shown by colour is the ring contrast. We see a correlation between η_r and δ_d , which for high-contrast rings is well modelled by the relation $\eta_r \sim 1.8 \delta_d^{1/2}$ predicted in equation (32).

We conclude that the survival of rings about massive central masses, as seen in the simulations post-compaction, Fig. 11, can be understood in terms of the analytic model, equation (28) and (30) as well as equations (34) with equation (32).

5 THE CENTRAL BODY OF RING GALAXIES

5.1 Baryons versus dark matter

It would be interesting to figure out the contributions of the different mass components to the central mass that determines the low values of δ_d and thus leads to long-lived rings. First, Fig. 16 shows the distribution of B/DM, the mass ratio of baryons to DM interior to the ring. In the case of a ring the masses are computed within the ring radius r_0 , and in the case of no-ring they are measured within $0.5R_d$, the average ring radius when there is a ring. Shown is the average of B/DM in bins within the M_v - z plane. We see that the

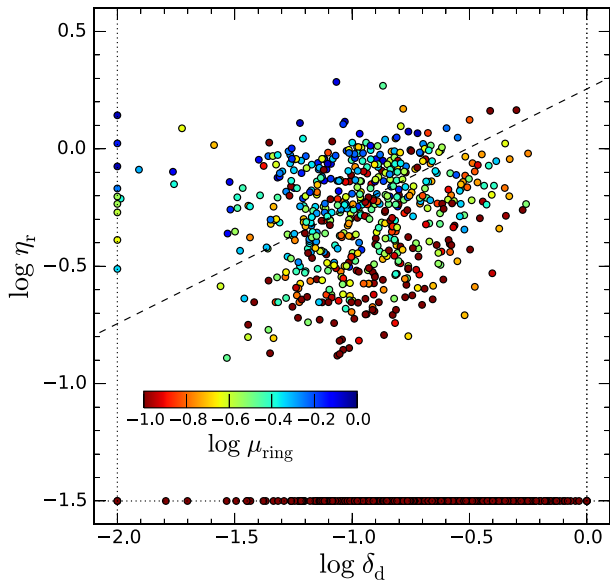


Figure 15. Analytic model versus simulations – ring thickness. Shown is the relative ring width $\eta_r = \Delta r/r$ versus δ_d for all simulated galaxies. The symbol colour represents ring contrast. Low values outside the box are put near the box axes (with many points accumulated at $\log \delta_d = -2$ and $\log \eta_r = -1.5$). We see that these quantities are marginally correlated. For high-contrast rings (blue and cyan) the correlation and the normalization are consistent with the relation $\eta_r \sim 1.8 \delta_d^{1/2}$ predicted in equation (32) (dashed line).

DM tends to dominate below the threshold mass near $M_v \sim 10^{11} M_\odot$ while the baryons tend to dominate above it. This reflects the major compactions to BNs near this characteristic mass. We note that in the regime that tends to populate rings, namely above the threshold mass and at $z < 1$, the average contributions of baryons and DM are comparable. We learn that the average post-compaction baryon dominance is typically marginal, by a factor of order unity and $\times 2.5$ at most.

To find out how DM may contribute to low values of δ_d and the associated high ring strength, Fig. 17 shows B/DM versus δ_d and versus μ_{ring} for all the simulated galaxies which show rings. We learn that the low values of $\delta_d < 0.3$, which are supposed to lead to rings, as well as the significant rings themselves, with $\mu_{\text{ring}} > 0.1$, say, could be associated with central bodies that are either dominated by baryons or by DM. Typically the contributions of the two components are comparable, with a slight preference for the DM. However, for massive galaxies B/DM ranges from 0.4 to 2.5. This implies that long-lived rings could appear even in cases where the central mass is dominated by DM with a negligible bulge. This is to be compared to observations. As mentioned in Section 6.2.1, both cases of baryon dominance and DM dominance are detected (Genzel et al. 2020).

The important contribution of the DM to the mass interior to the ring even after a major wet compaction event is partly because the wet compaction of gas induces an adiabatic contraction of stars and DM, and partly because the ring radius is significantly larger than the 1 kpc, or the effective radius R_e , within which the post-compaction baryons are much more dominant.

5.2 Nuggets: naked versus ringy, blue versus red

It is interesting to address the interplay between the strength of the ring and the nature of the mass in the central 1 kpc. Fig. 18 refers

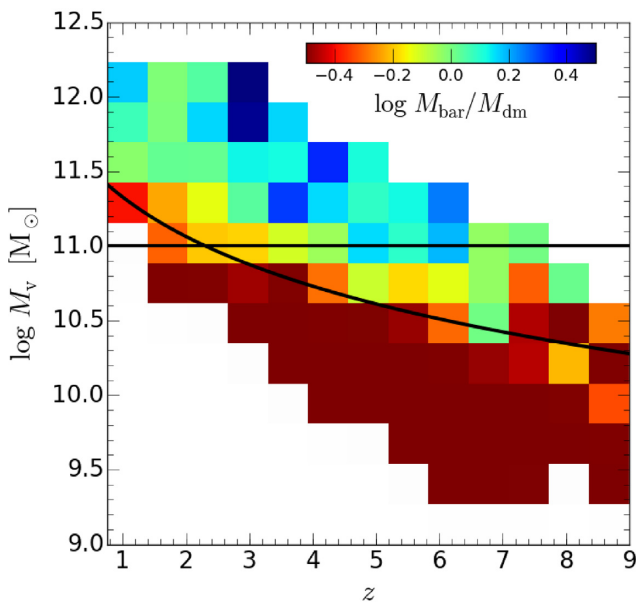


Figure 16. Nature of the central mass. Shown in bins within the M_v-z plane is the average of the baryon to DM ratio within the ring radius. For no-rings the radius is chosen to be $r_0 = 0.5 R_d$, the typical ring radius. The DM dominates below the characteristic mass of $\sim 10^{11} M_\odot$, while the baryons dominate above it, reflecting the transition due to the major compaction event. Nevertheless, even post-compaction the two components are comparable.

to this in terms of being a nugget, and if so whether it is an early star-forming BN or a late quenched red nugget. We learn from the left-hand panel that significant rings, e.g. $\mu_{\text{ring}} > 0.3$, pre-dominantly surround nuggets at their centres, defined by $\Sigma_{\text{s1}} > 10^9 M_\odot \text{ kpc}^{-2}$ (see Fig. 3). A larger fraction of the weaker rings have no central

nuggets (though they may still have large masses interior to the ring radius, which is typically several kpc, leading to a small δ_d). These no-nuggets are typically star-forming, pre-compaction and DM dominated.

Focusing on the galaxies with central nuggets, the right-hand panel of Fig. 18 shows the distribution of μ_{ring} for the nuggets only. We learn that ~ 40 per cent of the nuggets are naked, while ~ 60 per cent are surrounded by rings, with ~ 40 per cent having significant rings of $\mu_{\text{ring}} > 0.3$.

The red histogram refers to the fraction of red nuggets among the nuggets, defined by $\log \text{sSFR}_1 / \text{Gyr}^{-1} < -1$. We learn that among the significant rings, the nuggets are divided roughly half and half between quenched red nuggets and star-forming BNs, which tend to appear later and earlier after the compaction phase respectively.

These predicted fractions of rings with no central nuggets, of naked nuggets, and of blue versus red nuggets in galaxies that show rings, are to be compared to observations (see Ji et al., in preparation, and a preliminary discussion in Section 6).

5.3 Torques by a prolate central body

To complement the analytic model for disruptive mass transport, we note that it may be aided by torques exerted by a central body, stars or DM, if it deviates from cylindrical symmetry. Indeed, as can be seen in Fig. C1 in Appendix C (available in the Supporting Information), the VELA simulated galaxies tend to be triaxial, prolate pre-compaction and oblate post-compaction, showing a transition about the critical mass for BNs (Ceverino et al. 2015; Tomassetti et al. 2016). A similar transition has been deduced for the shapes of observed CANDELS galaxies (van der Wel et al. 2014; Zhang et al. 2019). The prolate pre-compaction bulge may exert non-negligible torques that could possibly disrupt the disc. In Appendix C (available in the Supporting Information), we learn from a very crude estimate that an extreme prolate central

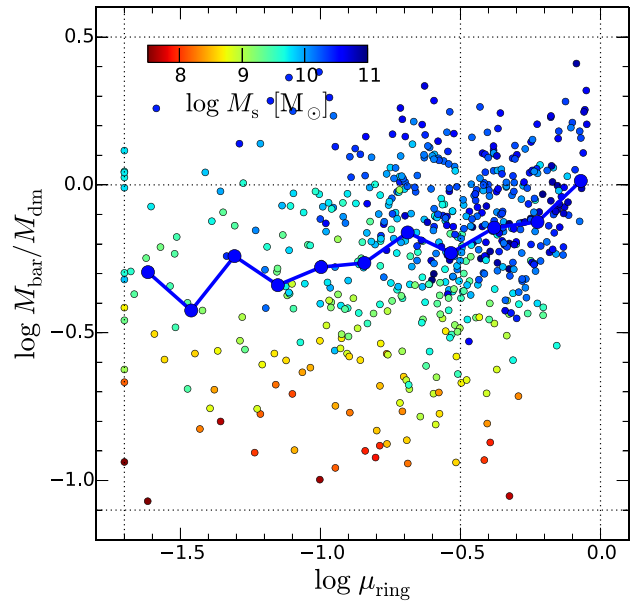
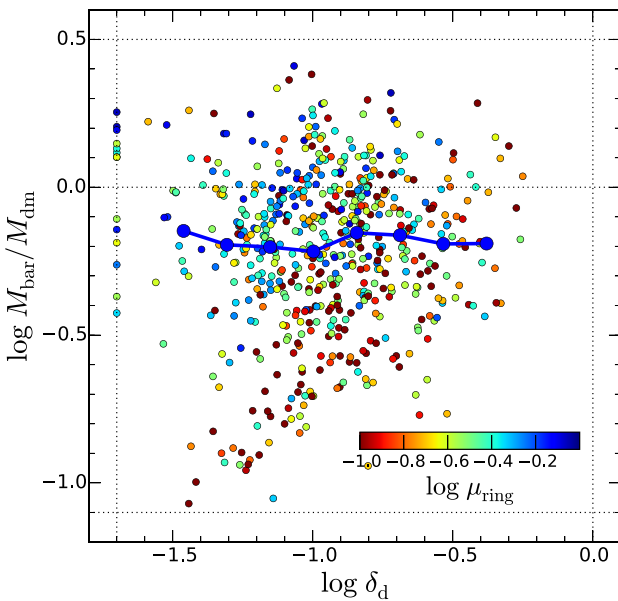


Figure 17. Baryons versus DM interior to the rings. Shown is the baryon-to-DM ratio versus δ_d (left) and μ_{ring} (right) for all galaxies with rings, with the median marked (blue). Low δ_d values (e.g. < 0.3) and the associated significant rings (e.g. $\mu > 0.1$ in this case) are obtained for a range of ratios, from baryon dominance by a factor $\times 2.5$ to DM dominance by a similar factor for massive galaxies, and by $\times 10$ for low-mass galaxies. In the median there is slightly more DM than baryons.

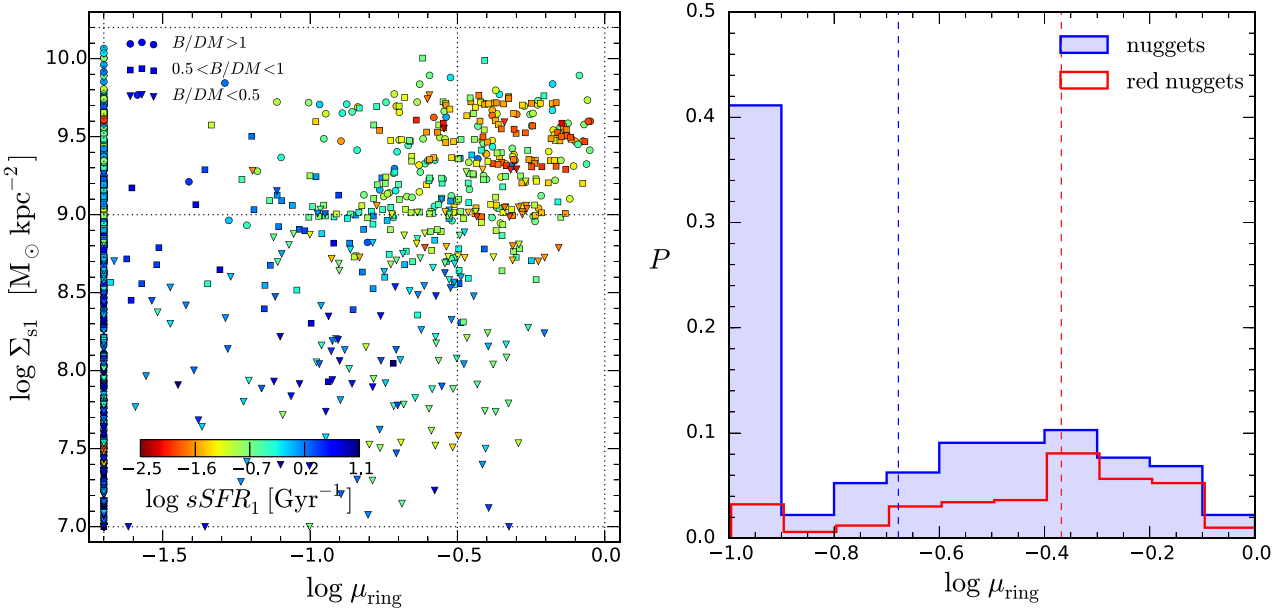


Figure 18. Nuggets and rings. Left: Stellar surface density within the inner 1 kpc, Σ_{S1} , versus ring gas mass excess, μ_{ring} , for all simulated galaxies. Nuggets are characterized by $\Sigma_{S1} > 10^9 M_\odot \text{ kpc}^{-2}$. Colour marks the sSFR within 1 kpc, with blue and red nuggets separated at $\log s\text{SFR}_1 / \text{Gyr}^{-1} \sim -1$. Right: The probability distribution of μ_{ring} for nuggets, obeying $\Sigma_{S1} > 10^9 M_\odot \text{ kpc}^{-2}$ (blue, shaded). The fraction of red nuggets, $\log s\text{SFR}_1 < -1$, is marked by the red histogram, with the difference between the blue and red histograms referring to the blue nuggets. We see on the left that pronounced rings tend to surround nuggets, while a significant fraction of the weaker rings have no central nuggets. Among the nuggets, on the right, ~ 40 per cent have significant rings of $\mu_{\text{ring}} > 0.3$, while ~ 40 per cent are naked with no rings. The nuggets inside rings are roughly half blue and half red nuggets.

body could have a non-negligible effect on the survival of a disc around it.

The central bulge, which tends towards an oblate shape (Fig. C1 in Appendix C, available in the Supporting Information), does not exert torques on masses orbiting in the major plane of the oblate system, but it does exert torques off this plane. An extreme oblate system, namely a uniform disc, yields values of $\Delta j/j \sim 0.1$ per quadrant of a circular orbit in a plane perpendicular to the disc and close to it (Danovich et al. 2015, fig. 16). This implies that the post-compaction central oblate body, above the critical mass for BNs, is not expected to significantly affect the AM of the disc and disrupt it.

6 PRELIMINARY COMPARISON TO OBSERVATIONS

6.1 Mock observations of simulated rings

6.1.1 Crude estimates

In order to crudely estimate H α fluxes for the simulated star-forming rings, we use our estimated SFR surface densities, averaged in the pronounced rings and in their giant clumps, of $\Sigma_{\text{SFR}} \sim (0.1-1) M_\odot \text{ yr}^{-1} \text{ kpc}^{-2}$. We then assume (1) a conversion to H α luminosity of $L_{\text{H}\alpha} (\text{erg s}^{-1}) = 1.8 \times 10^{41} \text{SFR}(M_\odot \text{ yr}^{-1})$ (Kennicutt et al. 2009), (2) an effective screen optical depth of $\tau_{\text{H}\alpha} = 0.73 \text{ Av}$ (Calzetti et al. 2000; Genzel et al. 2013), and (3) a typical visible extinction of $A_v = 1$ (e.g. Förster Schreiber et al. 2011a, b; Freundlich et al. 2013). This yields, for sources at $z = 1$, H α fluxes of $(1-10) \times 10^{-16} \text{ erg s}^{-1} \text{ cm}^{-2} \text{ arcsec}^{-2}$. Such values are in the ball park of those detected in resolved H α observations at $z \sim 1$ (e.g. Contini et al. 2012; Nelson et al. 2012; Genzel et al. 2013). Simulated rings traced by H α are also seen in Ceverino et al. (2017).

For crude estimates relevant for *HST* imaging, we note that for a source at $z \sim 1$ the F606W band of *HST* falls near 3000 Å and thus traces the rest-frame UV luminosity, which can serve as a proxy for star formation in the gaseous rings. Using the relation between UV luminosity and SFR based on Kennicutt (1998), corrected for a Chabrier (2003) initial mass function by a factor of $\times 1.8$, the SFR surface densities in the rings and the clumps, $\Sigma_{\text{SFR}} \sim (0.1-1) M_\odot \text{ yr}^{-1} \text{ kpc}^{-2}$ respectively, yield crudely estimated UV magnitudes of (23.4–20.9) mag arcsec $^{-2}$ without taking extinction into account. The fainter magnitudes may be more representative of the average surface brightness in the most pronounced rings in the simulations. Dust extinction in the UV is expected to lie between zero and 3 magnitudes (e.g. Buat & Xu 1996; Freundlich et al. 2013).

6.1.2 Mock ‘canceled’ images

In order to make more quantitative observable predictions for rings based on the simulated galaxies, we use mock 2D images that are generated for each given VELA simulated galaxy at a given time to mimic *HST* CANDELS images (CANDELization). As described in Snyder et al. (2015a) and Simons et al. (2019) (see MAST archive.stsci.edu/prepds/vela/), the stellar light is propagated through dust using the code SUNRISE. A spectral energy distribution (SED) is assigned to every star particle based on its mass, age and metallicity. The dust density is assumed to be proportional to the metal density with a given ratio and grain-size distribution. SUNRISE then performs dust radiative transfer using a Monte Carlo ray-tracing technique. As each emitted multiwavelength ray encounters dust mass, its energy is probabilistically absorbed or scattered until it exits the grid or enters the viewing aperture, selected here to provide a face-on view of the gas disc. The output of this process is the SED at each pixel. Raw mock images are created by integrating the SED in each pixel over

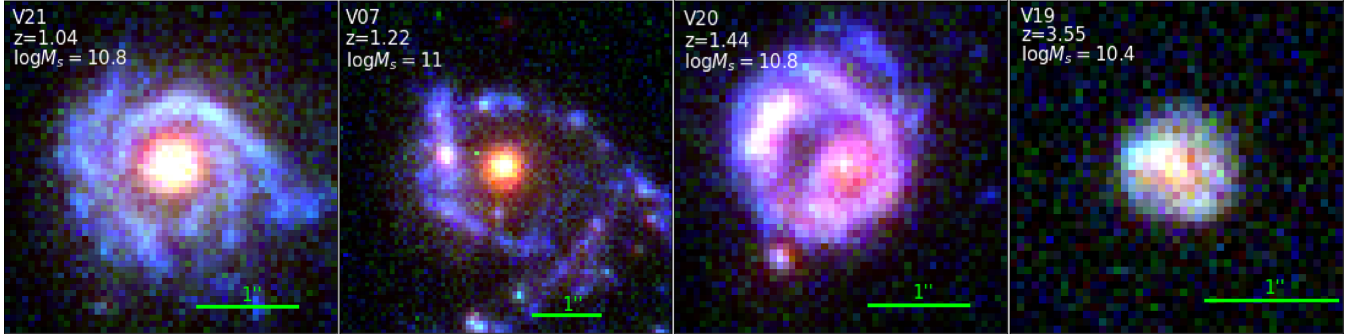


Figure 19. Mock images of simulated rings. Shown are three-colour rgb images showing blue rings about red massive bulges as ‘observed’ from the four simulated galaxies seen in Fig. 5. The corresponding mock images in the three filters F606W, F850LP, and F160W are shown in Fig. D2 in Appendix D (available in the Supporting Information). Dust is incorporated using Sunrise and the galaxy is observed face-on through the *HST* filters using the *HST* resolution and the noise corresponding to the CANDELS survey in the deep GOODS-S field.

the spectral response functions of the CANDELS ACS and WFC3 R and IR filters ($F606W$, $F850LP$, and $F160W$) in the observer frame given the redshift of the galaxy. These correspond at $z \sim 1\text{--}2$ to rest-frame UV , B to U , and R to V , respectively. Thus, the first two are sensitive to young stars while the third refers to old stars. The images are then convolved with the corresponding *HST* PSF at a given wavelength. Noise is added following Mantha et al. (2019), including random real noise stamps from the CANDELS data, to ensure that the galaxies are simulated at the depth of the real GOODS-S data and that the correlated noise from the *HST* pipeline is reproduced.

Fig. 19 shows the resultant mock rgb images for the four example VELA galaxies with rings, whose gas densities are shown in Fig. 5 and the corresponding profiles in Fig. 6. Fig. D2 in Appendix D (available in the Supporting Information) further shows the images of the same simulated galaxies in each filter separately. These are all post-compaction galaxies with $M_s \geq 10^{10.4} M_\odot$. At $z \sim 1\text{--}1.5$ the images show extended blue rings encompassing massive red bulges. The rings could be described as tightly wound spiral arms, which are sometimes not concentric about the bulge, and they tend to show giant clumps. With the added noise the ring structure becomes less obvious in the rgb picture of the $z = 3.55$ galaxy, though it is seen pretty clearly in the $F606W$ filter (Fig. D2 in Appendix D, available in the Supporting Information).

In order to make the predictions a bit more quantitative, Fig. 20 shows the SFR surface density profiles of the three VELA galaxies with clear rings at $z \sim 1\text{--}1.5$. These are compared to the light density profiles in the $F606W$ filter from the mock images shown in Fig. 19. The ring SFR density of $\sim 0.1 M_\odot \text{ yr}^{-1} \text{ kpc}^{-2}$ shows as a surface brightness of $\mu_{606} \sim 24 \text{ mag arcsec}^{-2}$, indicating only weak dust extinction. However, the predicted contrast in light between the ring and the interior is significantly smaller in the mock images. These are consistent with the crude estimates made at the beginning of this section.

6.1.3 Predictions for ALMA CO emission

The gas rings could be observable near the peak of star formation through their CO line emission. In particular, the CO(2-1) line at $\nu_{\text{rest}} = 230.538 \text{ GHz}$ is the lowest-excitation line observable with NOEMA and ALMA at $z \lesssim 2$. We assume (a) the Galactic value for the CO(1-0) conversion factor of molecular gas mass to luminosity, $\alpha_{\text{CO}} = 4.36 M_\odot / (\text{K km s}^{-1} \text{ pc}^2)$, (b) a conservative CO(2-1)/CO(1-0)

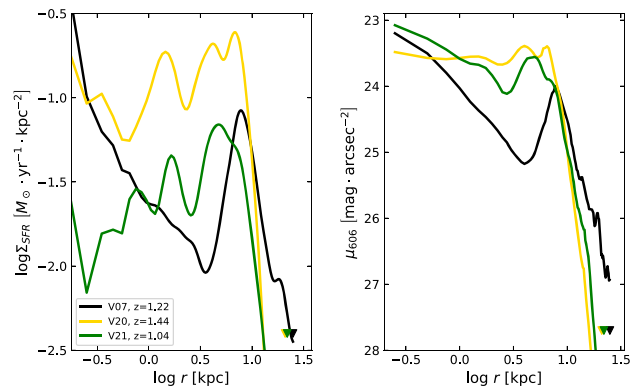


Figure 20. Rings in SFR versus luminosity from mock images of simulated galaxies. Shown are profiles of three example simulated galaxies with pronounced rings. Left: Face-on projected SFR surface density profiles from the simulations. Right: Light density profiles in the $F606W$ filter from the mock images shown in Fig. 19. The ring SFR density of $\sim 0.1 M_\odot \text{ yr}^{-1} \text{ kpc}^{-2}$ shows as $\sim 24 \text{ mag arcsec}^{-2}$, indicating weak dust extinction, but the predicted contrast between the ring and the interior is significantly smaller.

line ratio $r_{21} = 0.77$ (e.g. Daddi et al. 2015), and (c) the standard relation of Solomon et al. (1997) for converting intrinsic CO(2-1) luminosity into integrated flux (cf. also Freundlich et al. 2019). Then, the typical ring and clump molecular gas surface densities of $\Sigma_{\text{ring}} = 5 \times 10^7$ and $5 \times 10^8 M_\odot \text{ kpc}^{-2}$ respectively (assuming that the ring is dominated by molecular gas) yield integrated CO(2-1) line fluxes of 0.04 and $0.4 \text{ Jy km s}^{-1} \text{ arcsec}^{-2}$ at $z = 1$, and 0.10 and $1.0 \text{ Jy km s}^{-1} \text{ arcsec}^{-2}$ if the galaxy is put at $z = 0.5$.

We estimate that at $z = 1$, practical ALMA observation times per galaxy of $<10\text{h}$ would enable a detection of the dense clumps of such rings, but probably not the lower-density regions between the clumps. ALMA would need about 50h to detect the mean surface density of the rings with integrated SNR=6, assuming a line width of 200 km s^{-1} resolved by three channels. In order to visualize the detectability of rings by ALMA, Fig. 21 presents simulated CO(2-1) ALMA observations of the gas ring of V07 shown in Fig. 5. We see that if the galaxy is put at $z = 1$, parts of its ring would be traceable with 10h of ALMA but with a low signal to noise. At $z = 0.5$, the ring is detectable using 2 h of ALMA (60 h of NOEMA), and can be mapped with a higher signal-to-noise with 10h of ALMA.

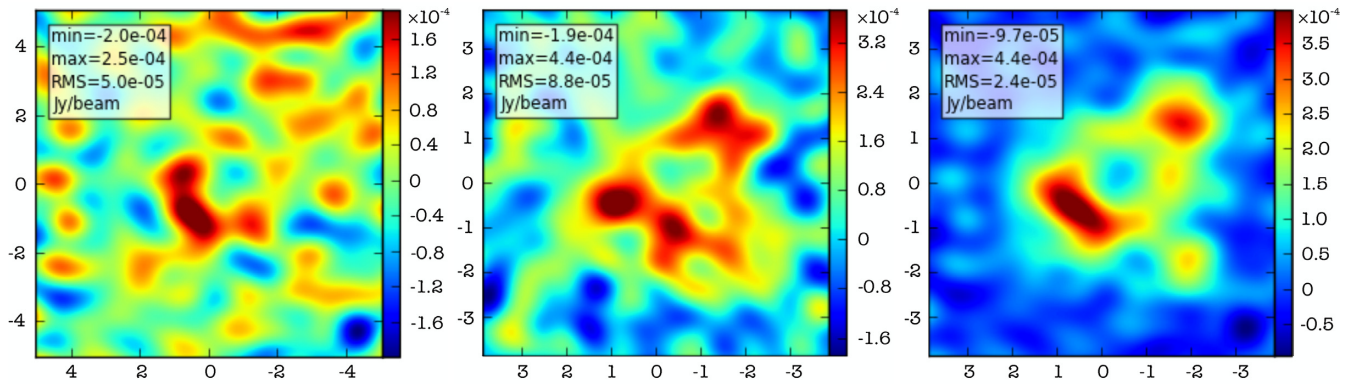


Figure 21. Mock ALMA images of a simulated ring. Shown are mock CO(2-1) ALMA observations of the V07 simulated gas ring (Fig. 5). Colour is in Jy per beam. Left: 10 h of observation with the galaxy at $z = 1$. Middle: 2 h at $z = 0.5$. Right: 10 h at $z = 0.5$. The simulations assumed the 12m array in Cycle 5 configuration 3 together with the Atacama Compact Array (ACA), yielding a spatial resolution of ~ 1.5 arcsec (12 kpc) and ~ 1 arcsec (6 kpc) at $z = 1$ and $z = 0.5$ respectively. The channel width was chosen to be 67 km s^{-1} in order to resolve the line width expected from the velocity dispersion (FWHM 200 km s^{-1}) with three channels. A typical precipitable water vapour level of 0.6 mm was assumed. The colour-map is in Jy per beam and distances are in arcsec. The simulations were carried out with the `simalma` task of CASA (McMullin et al. 2007).

6.2 Observed rings

6.2.1 In $H\alpha$

Genzel et al. (2014) detected a significant fraction of massive galaxies at $z \sim 2$ with extended $H\alpha$ star-forming rotating rings, most of which surrounding a central massive stellar bulge. This is consistent with the proposed formation and stabilization of the rings by central masses and the presence of post-compaction rings in our simulations. Then Genzel et al. (2020) and Genzel et al. (in preparation), following Genzel et al. (2017), utilizing rotation curves for 40 massive star-forming galaxies at $z = 0.6\text{--}2.7$ based on data from the 3D-HST/KMOS^{3D}/SINFONI/NOEMA surveys, verify the common existence of extended gas rings. They report that some of the rings surround massive compact bulges, typically with little DM mass within one or a few effective radii, while other rings surround less massive bulges but preferably with higher central DM masses (Genzel et al. 2020). This is qualitatively consistent with the model in Section 4 addressing the crucial role of a massive central body, which could either be a post-compaction massive bulge and/or a centrally dominant massive DM halo. It is also qualitatively consistent with our findings in the simulations (Section 5.1, Fig. 17) that the mass interior to significant rings in massive galaxies range from baryon dominance by up to a factor $\times 2.5$ to DM dominance by up to a similar factor or more.

In terms of the ring properties, in Genzel et al. (2014) the reported gas densities in the rings (e.g. their fig. 23) are $\Sigma_{\text{gas}} \sim 10^{8.6\text{--}9.0} M_{\odot} \text{ kpc}^{-2}$. This is higher than the average in the simulated rings and similar to the peak densities in the giant clumps within the simulated rings. The corresponding SFR densities deduced from the observed rings are $\Sigma_{\text{SFR}} \sim (1\text{--}2) M_{\odot} \text{ yr}^{-1} \text{ kpc}^{-2}$. This is again higher than the average across the simulated rings and comparable to the SFR densities in the simulated giant clumps. This difference may be partly due to the fact that the observed galaxies of $M_s \sim 10^{10.0\text{--}11.5} M_{\odot}$ are systematically more massive than the simulated galaxies with significant rings where $M_s \sim 10^{9.5\text{--}11.0}$ (Fig. B1 in Appendix B, available in the Supporting Information). It may also reflect the imperfection of the VELA-3 suite of simulations used here, which tend to underestimate the gas fractions (Fig. B1 in Appendix B, available in the Supporting Information). This is largely due to the relatively weak feedback incorporated, which leads to overestimated SFR at high redshifts.

Using AO-SINFONI $H\alpha$ spectroscopy as well as *HST* WFC3 multiwavelength imaging for $22 z \sim 2.2$ star-forming galaxies, Tacchella et al. (2015) revealed an inside-out quenching process, with the massive galaxies showing a pronounced peak in their stacked sSFR profile at $5\text{--}10$ kpc (their fig. 1), indicating rings, surrounding massive quenched bulges. Then, analysing dust obscuration in ten such galaxies, Tacchella et al. (2018) detected rings in the dust-corrected surface-density SFR profiles (their fig. 8), making sure that the SFR rings are real and not an artefact of missing SFR in the observed central regions. The corrected SFR surface densities are in the range $0.1\text{--}1 M_{\odot} \text{ kpc}^{-2}$, similar to the simulation results.

6.2.2 In HST images

In a pioneering study, Elmegreen & Elmegreen (2006) showed *HST*-ACS V_{606} -band images of 24 galaxies in the GEMS and GOODS surveys, in the redshift range $0.4\text{--}1.4$. They detected 9 rings and 15 partial rings, each containing a few giant clumps and surrounding a massive bulge, with no obvious bars or grand-design spiral structure. Several observed ‘chain’ galaxies, showing similar clumps, were identified as the edge-on analogues of the more face-on ring galaxies.

The general impression from crude visual inspections of the more recent CANDELS-*HST* galaxies used to be that they are not showing rings, somehow ignoring the Elmegreen & Elmegreen (2006) results and leading to a common notion that blue and red nuggets tend to be ‘naked’. Naked nuggets were indeed reported at $z \sim 1\text{--}2$ (e.g. Williams et al. 2014; Lee et al. 2018). This impression might have emerged from rest-frame optical images, focusing on old stars, rather than rest-frame UV that reflects star formation. In contrast, deeper CANDELS images focusing on rest-frame UV did show hints for star-forming rings around massive bulges (e.g. Dunlop, private communication). Recall that in Section 5.2, we found in the simulations that while ~ 40 per cent of the nuggets are expected to be totally naked, another ~ 40 per cent of the nuggets are expected to have significant rings of $\mu_{\text{ring}} > 0.3$.

Indeed, an ongoing search in the deeper GOODS fields (Ji, Giavalisco, Dekel et al., in prep.) reveals many star-forming rings about massive bulges. The rings are visually identified in the F606W bandpass, which is deep enough and relatively sensitive to young stars at $z \sim 1$, and the images are then studied in the

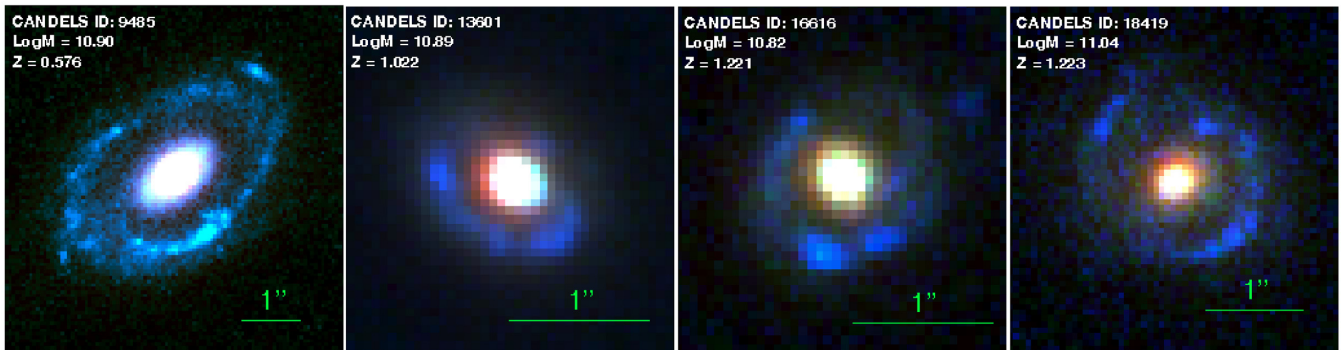


Figure 22. Observed rings. Shown are three-colour rgb images from the deepest, GOODS fields of CANDELS, displaying extended blue rings about red massive bulges. The corresponding images in the three filters F606W, F850LP, and F160W are shown in Fig. D3 in Appendix D (available in the Supporting Information). The average F606W surface brightness in the rings is 24.6, 24.7, 25.6, and 25.5 mag arcsec $^{-2}$ in rings id 9485, 13601, 16616, and 18419, respectively. The identified rings with bulges are a non-negligible fraction of the galaxies with masses $M_s > 10^{10.5} M_\odot$ at $z = 0.5\text{--}1.2$ (Ji et al., in preparation).

complementary F850LP and F160W filters, the latter capturing older stars. Our preliminary inspections indicate that, among the galaxies of $M_s > 10^{10.5} M_\odot$ at $z = 0.5\text{--}1.2$, a non-negligible fraction of order ~ 10 per cent clearly show blue star-forming, clumpy rings, typically surrounding a massive bulge, which is either star forming or quenched. Clearly, this detected fraction of rings is a far lower limit, limited to galaxies of low inclinations, sufficiently extended rings, high-contrast rings and bright enough rings that are more easily detected at $z \lesssim 1$. Furthermore, a large fraction of the galaxies were eliminated from the ring search based on a pronounced spiral structure, while our theoretical understanding in Section 4 is that the spiral structure is intimately linked to the presence of a ring.

In our simulations, we read from Fig. 11 that ~ 24 per cent of the galaxies are expected to have pronounced rings of $\mu_{\text{ring}} > 0.5$. Focusing on massive galaxies at $z \sim 1$, we read from the colours in Fig. B2 in Appendix B (available in the Supporting Information) that the fraction relevant to the range of masses and redshifts where the observations were analysed is closer to ~ 30 per cent. In the range $z = 1.4\text{--}2$, this fraction is reduced to ~ 10 per cent. According to Fig. 10, the average ring strength in massive galaxies at $z \sim 1$ is indeed just below $\mu_{\text{ring}} = 0.5$. Given the underestimate in the observational detection of rings, the numbers in the simulations and the observations may be in the same ball park.

Visualization of such observed rings is provided by Fig. 22, which displays four preliminary example rgb images of CANDELS galaxies showing rings, with masses $M_s > 10^{10.8} M_\odot$ at $z = 0.58\text{--}1.22$ as marked in the figure. Fig. D3 in Appendix D (available in the Supporting Information) shows the same galaxies in the three filters separately. These observed images show rings that qualitatively resemble the mock images from the simulated galaxies shown in Fig. 19. The average F606W surface brightness in the rings is 24.6, 24.7, 25.6, 25.5 mag arcsec $^{-2}$ in rings id 9485, 13601, 16616, 18419, respectively. These are in the ball park of the ~ 24 mag arcsec $^{-2}$ of the most pronounced mock rings shown in Fig. 20, given the uncertainties in the simulations, their mock images and the way the ring surface brightness is estimated as well as in the surface brightness deduced for the observed rings. Both the simulations and the observations show massive bulges, though two of the observed bulges are blue while all the four displayed simulated bulges are redder. We recall from Section 5.2 that among the significant simulated rings with central nuggets about one half are red nuggets, consistent with what is indicated observationally.

These pictures of observed high-redshift rings in CANDELS are just a sneak preview of a detailed analysis. The challenge to be addressed is to evaluate the effect of dust on the appearance of rings and bulges in these images. If these rings are real and not artefacts of dust absorption in the inner regions, they would be qualitatively compatible with the H_α observations of Genzel et al. and along our theoretical understanding of extended star-forming gas rings about BNs or red nuggets. Complementary spectroscopic studies would explore the ring kinematics and dynamics.

6.2.3 At low redshifts

Interestingly, Salim et al. (2012) found that most low-redshift ‘Green-Valley’ galaxies, at the early stages of their quenching process, or S0-type galaxies, consist of massive quenched bulges surrounded by star-forming rings that are seen in rest-frame UV. Even closer to home, M31 and the Sombrero galaxy are known to show very pronounced dusty rings in IR surrounding a massive stellar bulge and disc. While our simulations refer more explicitly to high-redshift, stream-fed gaseous, unrelaxed galaxies in which the conditions for ring formation may be different from the more secular $z = 0$ galaxies, we note that the high- z rings tend to appear after the major compaction events, which are the early stages of quenching, namely in the Green Valley (Tacchella et al. 2016b). Our general analysis in Section 4 of ring stabilization by a central mass through a low δ_d , and the considerations based on t_{inf} versus t_{acc} and t_{sfr} , may be relevant with some modifications also for explaining the longevity of the low-redshift rings. Some of the low-redshift rings may be the descendants of rings that formed after an earlier compaction event and remained in the Green Valley due to the continuous star formation in the long-lived rings. This is alongside the traditional modelling of rings at resonances in secular discs or as outcomes of collisions.

7 DISCUSSION: OTHER MECHANISMS FOR RING FORMATION

We discussed here a picture where the high-redshift rings are long-lived dynamic features that are fed by high-AM cold gas streams, where their torque-driven mass transport inwards is suppressed by a massive central body and where the gas is depleted efficiently from the interior disc by star formation and outflows. Low-redshift rings are commonly assumed to be resonant features in secular evolution,

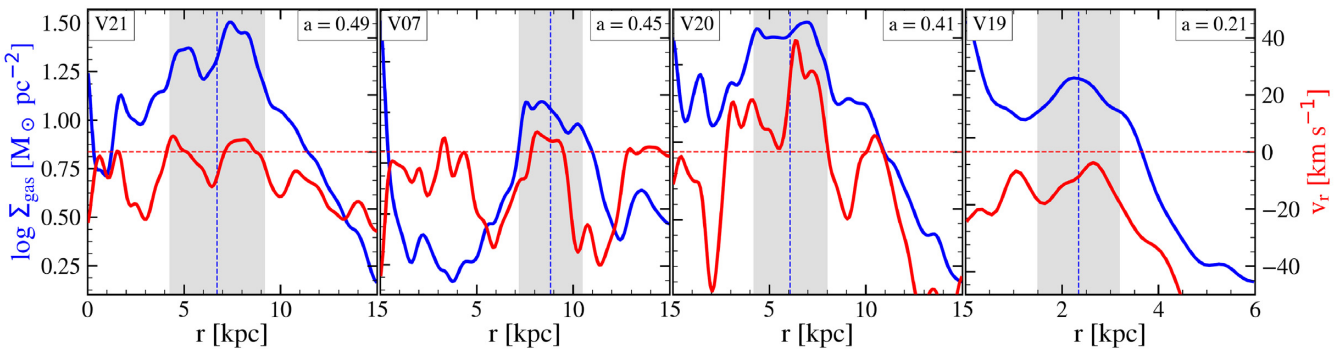


Figure 23. Testing whether the rings may reside at resonant radii. Shown (in red) is the radial profile of radial velocity in the disc plane, mass-weighted averaged over circular rings, for the four cases of strong rings in the VELA simulations. Shown in comparison (in blue) is the gas surface density profile, with the ring radius and width of its main body marked by a vertical line and a shaded area. In all four cases, we see inward averaged radial velocity both interior and exterior to the ring, indicating that the rings do not reside at CR or at the OLR.

or they are proposed to be formed by a collision with another galaxy (rings types O and P respectively, Few & Madore 1986). We discuss here the potential applicability of these ring-forming mechanisms to the high-redshift rings that we see in our simulations.

7.1 Rings at resonances in secular discs

In our analysis in Section 4, we assumed that the high-redshift discs, which are continuously fed by intense streams and are growing massive bulges, are subject to significant variations of the gravitational potential and are not in their secular phase yet. We further assumed that if the spiral structure has a semi-well-defined pattern speed Ω_p , the gas angular velocity in the main disc is larger, $\Omega(r) > \Omega_p$, namely the main disc is inside the co-rotation radius (CR). This is typically the case in low- z grand-spiral galaxies, where the arms are trailing and the gas is indicated to cross the arms from the inside, where it is compressed and it forms stars. This is based, e.g. on the observation that the IR light, characteristic of the first Myr of star formation, is emitted from the inner, back side the arms, while the UV, associated with stars of ~ 100 Myr, tends to be emitted from the arms and their outer, front side. Inside CR, the torques by trailing arms induce AM transport outwards, associated with mass transport inwards (Section 6.1.3.d of BT).

On the other hand, open spiral structure, and especially strong bars, in relaxed discs undergoing secular evolution at low redshifts, where there is a constant pattern speed Ω_p , may be responsible for rings of gas at resonance radii (e.g. de Vaucouleurs 1959; Buta & Combes 1996; Buta 2017a, b). Is it possible that the rings we see in the high- z simulated galaxies reside in resonance radii despite their unrelaxed nature? One such resonance is at CR, where $\Omega(r) = \Omega_p$, and where no torques are acting to induce mass transport inward or outward. More common at $z = 0$ is a ring at the Outer Lindblad Resonance (OLR), at a radius outside co-rotation where $m [\Omega(r) - \Omega_p] = -\kappa$ with the epicyclic frequency $\kappa^2 = r d\Omega^2/dr + 4\Omega^2$. The torques by the spiral structure outside CR induce mass transport outwards, pushing the gas to accumulate in the OLR. The radial velocities interior to the ring and exterior to it can thus indicate whether the rings may be residing in a resonance radius.

In order to address this distinguishing feature, Fig. 23 shows the radial profile of radial velocity in the disc plane, mass-weighted averaged over circular rings, for our four fiducial cases of strong rings in the VELA simulations. Shown in comparison is the gas surface density profile, with the ring radius and width of its main body marked. In

all four cases, we see inward averaged radial velocity both interior and exterior to the ring. Naturally, when inspecting the 2D maps of radial velocity, there are some angular directions where an outward velocity is detected interior or exterior to the ring. This is as expected from a rather perturbed, turbulent disc. The radial velocities roughly range from -100 km s^{-1} to $+50 \text{ km s}^{-1}$ (where the general rotation velocity is $\sim 300 \text{ km s}^{-1}$). We interpret the fact that the average radial velocity is inwards both interior and exterior to the ring as an indication for the rings not to reside at resonant radii, neither at CR nor at the OLR.

The simulated galaxies at high redshift typically do not show massive bars or grand-design spiral structure. This is consistent with the observed low abundance of bars at high redshifts. According to an analysis of the COSMOS field by Sheth et al. (2008), while about 30 per cent of the $z = 0$ disc galaxies show strong bars (65 per cent show any bars), this fraction drops to 10 per cent (20 per cent) already at $z = 0.84$. Indeed, Elmegreen & Elmegreen (2006) report the absence of obvious bars or open spiral structure in the ring galaxies that they were the first to identify in the GOODS fields at $z = 0.4\text{--}1.4$. This implies that the most likely drivers of resonance rings, namely bars or open spirals, are missing in the high-redshift ring galaxies. Nevertheless, possible tidal effects from a massive companion, or oval distortions, as alternatives to a bar in driving resonances (Buta & Combes 1996), are not strictly ruled out in all cases.

Additional evidence not supporting the possibility that the simulated high-redshift rings are associated with resonant radii is provided by the facts that (a) the metallicity in the simulated rings is lower than in the interior disc as seen in Fig. 6, hinting for an external origin of the gas, (b) the rings are actually seen to be fed by inflowing cold streams, and (c) the rings pre-dominantly consist of gas as opposed to stars.

We can report yet another preliminary test for being inside the CR. For discs at the early post-compaction phase, where one could identify spiral structure, we plotted the spatial distribution of very young stars of 0–60 Myr (assumed to be responsible for IR emission) versus that of somewhat less young stars of 80–120 Myr (assumed to dominate the UV emission). We find visual evidence for the younger population to lie inside the arms, indicating that the gas is crossing the trailing arm from the inside as it forms stars, which is another evidence for being inside CR, similar to the cases of grand spirals at low redshift. A further, more detailed study of the high- z rings in the context of the pattern speed and the resonant radii is beyond the scope of the current paper and is deferred to a future study.

7.2 Collisional ring galaxies

Rings could be nearly symmetrical density waves that are driven into a disc as a result of a bulls-eye collision with another galaxy, as reviewed by Appleton & Struck-Marcell (1996) following the original proposals (Lynds & Toomre 1976; Theys & Spiegel 1977; Toomre 1978). The prototypical low-redshift example is the Cartwheel galaxy, where a suspect perturbing galaxy is possibly identified in the image. Ring galaxies in cosmological simulations have been widely studied in the context of collisions (e.g. D’Onghia, Mapelli & Moore 2008; Snyder et al. 2015b; Elagali et al. 2018; Renaud et al. 2018). The collision scenario for ring formation is supposed to be associated with inside-out ring buildup from stars and gas, an outward ring velocity, and a relatively short ring lifetime of a few hundred Myr (e.g. Mapelli et al. 2008a, b). Recently, a collision has been proposed as a possible interpretation for an observed ring galaxy at $z = 2.19$ (Yuan et al. 2020), largely based on marginal evidence for an outward radial velocity of the ring.

Most of the ring galaxies seen in our simulations at high redshifts are not likely to be driven by collisions for several reasons, as follows. First, the simulated rings typically do not show outward radial velocities. In this respect galaxy V20 shown in Fig. 23 at $a = 0.41$ is an exception, with the ring moving outward at $\leq 40 \text{ km s}^{-1}$. Instead, the rings (including V20) show inward velocities interior and exterior to the ring, as seen in Fig. 23, while a collision origin would imply outward velocities also interior to the ring. Second, the metallicity in the rings is lower than in the disc interior to the rings, as seen in Fig. 6, indicating that they do not emerge from the inner disc but are rather fed by external fresh accretion. Indeed, the rings are typically seen to be associated with visible incoming cold streams. Third, the simulated rings are primarily gaseous, while the collisional rings are expected to contain a significant component of stars as well. Finally, some of the rings are long lived, beyond the relatively short lifetimes expected for collisional rings.

Still, since we have demonstrated that the longevity of the rings in our simulations is associated with compaction-driven central masses, and since a significant fraction of the compaction events are actually triggered by mergers, our proposed scenario is also associated with mergers, even if in an indirect way. This calls for a further study of the interplay between the scenario discussed here and the collision scenario for ring formation.

7.3 The effect of AGN feedback on rings

The robustness of our results based on the VELA simulations should be examined by analysing rings in other cosmological simulations, based on different codes with different resolutions, and different subgrid recipes for processes such as star formation and feedback.

In particular, since the current VELA simulations on which our ring analysis is based do not include black holes and the associated AGN feedback, one may worry whether AGN feedback could damage the rings and possibly eliminate them altogether. Indeed, strong AGN activity is predicted and observed in star-forming galaxies above the golden mass, where extended rings form (e.g. Förster Schreiber et al. 2019; Dekel et al. 2019b).

In an ongoing work, we are searching for and analysing high-redshift rings in cosmological simulations that do include AGN feedback. For example, the TNG simulations that do incorporate rather strong AGN feedback would be appropriate for such an exploration of the AGN effects on the rings. We can report that a preliminary visual inspection of images of gas and SFR surface density of TNG galaxies at $z \sim 1\text{--}2$ indicates a large abundance

of rings, which seem to largely resemble the VELA rings studied here. This indicates that the rings survive the AGN feedback, possibly because the ejected AGN energy and momentum are largely collimated in the polar disc and ring direction.

The significant abundance of observed rings above the golden mass at $z \sim 1\text{--}2$, as summarized in Section 6.2, by itself provides evidence for the survivability of the rings under AGN feedback. The theoretical and observational aspects of the interplay between AGN activity and the rings are to be quantitatively explored.

8 CONCLUSION

In Dekel et al. (2020) we argued, analytically and using simulations, that galactic gas discs are likely to be long-lived only in DM haloes of mass above a threshold of $\sim 2 \times 10^{11} M_\odot$, corresponding to a stellar mass of $\sim 10^9 M_\odot$, with only little dependence on redshift. In haloes of lower masses, the gas does not tend to settle into an extended long-lived rotating disc, as several different mechanisms act to drastically change the angular momentum and thus disrupt the disc. First, the AM is predicted to flip on a time-scale shorter than the orbital time-scale due to mergers associated with a pattern-change in the cosmic-web streams that feed the galaxy with AM. Second, in this pre-compaction low-mass regime (e.g. Zolotov et al. 2015), violent disc instability exerts torques that drive AM out and mass in, thus making the disc contract in a few orbital times (e.g. Dekel et al. 2009b). Third, in this regime the central DM and stellar system tend to be prolate (e.g. Tomasetti et al. 2016) and thus capable of producing torques that reduce the AM of the incoming new gas.

Furthermore, supernova feedback is expected to have a major role in disrupting discs below the critical mass. This emerges from a simple energetic argument that yields an upper limit of $V_v \sim 100 \text{ km s}^{-1}$ for the DM halo virial velocity (i.e. potential well) within which supernova feedback from a burst of star formation could be effective in significantly heating up the gas (Dekel & Silk 1986). Supernova feedback stirs up turbulence that puffs up the disc and it suppresses the supply of new gas with high AM (Tollet et al. 2019), possibly even ejecting high-AM gas from the disc outskirts. As argued in section 3 of Dekel et al. (2020), supernova feedback determines the mass dependence of the stellar-to-halo mass ratio that enters into the merger rate and thus affects the frequency of disc disruption by spin flips. Finally, supernova feedback has a major role in confining the major compaction events to near or above the golden mass (Dekel et al. 2019b), and, as shown in the current paper, these compaction events are responsible for the formation and longevity of extended rings.

Above this golden mass, the disruptive mergers are less frequent and are not necessarily associated with a change in the pattern of the feeding streams, allowing the discs to survive for several orbital times. In parallel, the effects of supernova feedback are reduced due to the depth of the halo potential well.

The main issue addressed in this paper is the post-compaction formation of long-lived rings above a critical mass, similar to the golden mass for supernova feedback and merger-driven disc flips. We showed using the simulations that in the post-compaction regime, typically after $z \sim 4$, the inflowing high-AM streams from the cosmic web settle into extended discs that evolve into long-lived rings. Using measures of ring strength in each simulated galaxy, such as contrast and mass fraction, we quantified the tendency of the rings to appear after the major compaction events and above the corresponding mass threshold, and showed that their strength is growing with time and mass with respect to the BN phase.

In order to understand the ring longevity, we have worked out the torques exerted by a tightly wound spiral structure on the disc outskirts. We found that the time-scale for inward mass transport for a ring of constant relative width is roughly $t_{\text{inf}} \sim 6 \delta_{d,0.3}^{-3} t_{\text{orb}}$, and the spiral pitch angle is given by $\tan \alpha \sim \delta_d$, where δ_d is the cold-to-total mass ratio interior to the ring. By comparing this to the time-scales for external accretion and interior SFR, t_{acc} and t_{sfr} , requiring ring replenishment $t_{\text{inf}} > t_{\text{acc}}$ and depletion of the interior, $t_{\text{inf}} > t_{\text{sfr}}$, we learned that a ring forms and survives when $\delta_d < 0.3$. The required low values of δ_d are most naturally due to the post-compaction massive bulge. A similar extended long-lived ring would appear about a massive DM dominated central region, which could be another reason for a reduced δ_d . There is a lower bound on the values of δ_d that allow rings when the low values are driven by a low gas fraction, because the ring phenomenon is primarily gaseous. Once the ring develops a high contrast, the inward transport rate becomes longer than the Hubble time and all other relevant time-scales. The ring remains intact but it gradually weakens due to the weakening accretion rate with cosmological time and the gradual ring depletion into stars. The long-lived ring could be Toomre unstable, with giant clumps forming stars, as long as it is fed by high-AM cold gas streams.

The high- z rings seen in our simulations are unlikely to be associated with resonant radii as in secular discs at low redshifts because the high- z galaxies are not in a secular phase, they show no bars or open spirals, the radial velocities interior and exterior to the ring tend to be inwards, the ring gas is indicated to come from external accretion based on its low metallicity and the association with inflowing streams, and the rings are pre-dominantly gaseous, not stellar. The simulated rings are also not likely to originate from collisions a la the Cartwheel galaxy based on the very same properties, including the fact that in most cases the rings are not moving outward, and they live for more than a few hundred Myr.

In order to allow first crude comparisons of the simulated rings-about-bulges to observations, we generated mock images from ringy simulated galaxies that mimic multicolour *HST* images in CANDELS deep fields including dust extinction. The pronounced rings at $r \sim 10$ kpc are expected to form stars at a surface density of $\Sigma_{\text{SFR}} \sim (0.1 - 1) M_\odot \text{ yr}^{-1} \text{ kpc}^{-2}$. This corresponds at $z \sim 1$ to an average surface brightness of ~ 24 mag arcsec $^{-2}$ in the F606W filter, corresponding to rest-frame UV, with weak dust extinction. We also showed mock ALMA images of CO(2-1) emission, indicating that $z \sim 1$ rings would be detectable but at a low signal to noise with 10h of ALMA observations. A ring at $z \sim 0.5$ would be detectable at a higher signal to noise even with a few-hour exposure.

Observational studies including H α kinematics (Genzel et al. 2014, 2017, and work in progress) show gaseous star-forming clumpy rings around massive bulges or DM dominated centres in a significant fraction of $z \sim 1-2$ galaxies above the threshold mass. This is qualitatively consistent with our theoretical understanding that a massive central mass is expected to support an extended ring for long times. It is also along the lines of the prediction of major compaction events that generate massive bulges typically above a similar threshold mass. In our simulations we find that for massive galaxies with pronounced rings, the baryon-to-DM ratio interior to the ring ranges from 0.4 to 2.5.

We provided a sneak preview of an ongoing study of rings in the deepest fields of the *HST*-CANDELS multicolour imaging survey (Ji et al., in preparation). The sample galaxies shown qualitatively resemble the mock images from the simulations, with star-forming clumpy rings about massive bulges. Our preliminary results indicate

that, indeed, when observed deep enough, a non-negligible fraction of the galaxies of $M_s > 10^{10.5} M_\odot$ at $z \sim 0.5-3$ show blue rings about massive bulges.

In our simulations, strong rings typically have nuggets in their 1 kpc centres, of which roughly half are star-forming BNs and the other half are quenched red nuggets. Among the nuggets, about half are naked, and the other half are surrounded by significant rings. There are preliminary indications that these predictions are in the ball park of the observed ring and nuggets populations, but this is a subject for future studies.

ACKNOWLEDGEMENTS

We acknowledge Greg Snyder and Raymond Simons for the CANDELIZED mock images. We thank Francoise Combes, Jim Dunlop, Sandy Faber, Reinhard Genzel, David Koo, Gary Mammon, Christophe Pichon, Samir Salim, and Sandro Tacchella for stimulating interactions. This work was partly supported by the grants Germany–Israel GIFI-1341-303.7/2016, DIP Germany–Israel Project Cooperation Foundation STE1869/2-1 GE625/17-1, I-CORE Program of the PBC/ISF 1829/12, US–Israel BSF 2014-273, and NSF AST-1405962. The cosmological VELA simulations were performed at the National Energy Research Scientific Computing Center (NERSC) at Lawrence Berkeley National Laboratory and at NASA Advanced Supercomputing (NAS) at NASA Ames Research Center. Development and analysis have been performed in the astro cluster at HU.

REFERENCES

- Anglés-Alcázar D., Faucher-Giguère C.-A., Quataert E., Hopkins P. F., Feldmann R., Torrey P., Wetzel A., Kereš D., 2017, *MNRAS*, 472, L109
- Appleton P. N., Struck-Marcell C., 1996, *Fundam. Cosm. Phys.*, 16, 111
- Barro G. et al., 2013, *ApJ*, 765, 104
- Barro G. et al., 2014a, *ApJ*, 791, 52
- Barro G. et al., 2014b, *ApJ*, 795, 145
- Barro G., Trumpp J., Koo D. C., Dekel A., Kassin S. A., Kocevski D., Faber S. M., Canadas, 2015, in American Astronomical Society Meeting Abstracts, Vol. 225, p. 111.07
- Barro G. et al., 2016a, *ApJ*, 820, 120
- Barro G. et al., 2016b, *ApJ*, 827, L32
- Barro G. et al., 2017a, *ApJ*, 840, 47
- Barro G. et al., 2017b, *ApJ*, 851, L40
- Binney J., Tremaine S., 2008, *Galactic Dynamics*. Princeton Univ. Press, Princeton, NJ (BT)
- Birnboim Y., Dekel A., 2003, *MNRAS*, 345, 349
- Bournaud F., Elmegreen B. G., Elmegreen D. M., 2007, *ApJ*, 670, 237
- Bournaud F., Dekel A., Teyssier R., Cacciato M., Daddi E., Juneau S., Shankar F., 2011, *ApJ*, 741, L33
- Bower R. G., Schaye J., Frenk C. S., Theuns T., Schaller M., Crain R. A., McAlpine S., 2017, *MNRAS*, 465, 32
- Bruce V. A. et al., 2012, *MNRAS*, 427, 1666
- Buat V., Xu C., 1996, *A&A*, 306, 61
- Buta R. J., 2017a, *MNRAS*, 471, 4027
- Buta R. J., 2017b, *MNRAS*, 470, 3819
- Buta R., Combes F., 1996, *Fundam. Cosm. Phys.*, 17, 95
- Calzetti D., Armus L., Bohlin R. C., Kinney A. L., Koornneef J., Storchi-Bergmann T., 2000, *ApJ*, 533, 682
- Cattaneo A., Dekel A., Devriendt J., Guiderdoni B., Blaizot J., 2006, *MNRAS*, 370, 1651
- Ceverino D., Klypin A., 2009, *ApJ*, 695, 292
- Ceverino D., Dekel A., Bournaud F., 2010, *MNRAS*, 404, 2151
- Ceverino D., Dekel A., Mandelker N., Bournaud F., Burkert A., Genzel R., Primack J., 2012, *MNRAS*, 420, 3490

- Ceverino D., Klypin A., Klimek E. S., Trujillo-Gomez S., Churchill C. W., Primack J., Dekel A., 2014, *MNRAS*, 442, 1545
- Ceverino D., Primack J., Dekel A., 2015, *MNRAS*, 453, 408
- Ceverino D., Primack J., Dekel A., Kassin S. A., 2017, *MNRAS*, 467, 2664
- Chabrier G., 2003, *PASP*, 115, 763
- Codis S., Pichon C., Devriendt J., Slyz A., Pogosyan D., Dubois Y., Sousbie T., 2012, *MNRAS*, 427, 3320
- Contini T. et al., 2012, *A&A*, 539, A91
- Daddi E. et al., 2015, *A&A*, 577, A46
- Damjanov I. et al., 2009, *ApJ*, 695, 101
- Damjanov I. et al., 2011, *ApJ*, 739, L44
- Danovich M., Dekel A., Hahn O., Teyssier R., 2012, *MNRAS*, 422, 1732
- Danovich M., Dekel A., Hahn O., Ceverino D., Primack J., 2015, *MNRAS*, 449, 2087
- Dekel A., Birnboim Y., 2006, *MNRAS*, 368, 2
- Dekel A., Burkert A., 2014, *MNRAS*, 438, 1870
- Dekel A., Silk J., 1986, *ApJ*, 303, 39
- Dekel A. et al., 2009a, *Nature*, 457, 451
- Dekel A., Sari R., Ceverino D., 2009b, *ApJ*, 703, 785
- Dekel A., Zolotov A., Tweed D., Cacciato M., Ceverino D., Primack J. R., 2013, *MNRAS*, 435, 999
- Dekel A., Sarkar K. C., Jiang F., Bournaud F., Krumholz M. R., Ceverino D., Primack J. R., 2019a, *MNRAS*, 488, 4753
- Dekel A., Lapiner S., Dubois Y., 2019b, preprint ([arXiv:1904.08431](https://arxiv.org/abs/1904.08431))
- Dekel A., Ginzburg O., Jiang F., Freundlich J., Lapiner S., Ceverino D., Primack J., 2020, *MNRAS*, 493, 4126
- de Vaucouleurs G., 1959, *Handbuch der Physik*, 53, 275
- D'Onghia E., Mapelli M., Moore B., 2008, *MNRAS*, 389, 1275
- Dubois Y., Volonteri M., Silk J., Devriendt J., Slyz A., Teyssier R., 2015, *MNRAS*, 452, 1502
- Elagali A., Lagos C. D. P., Wong O. I., Staveley-Smith L., Trayford J. W., Schaller M., Yuan T., Abadi M. G., 2018, *MNRAS*, 481, 2951
- Elmegreen B. G., Bournaud F., Elmegreen D. M., 2008, *ApJ*, 688, 67
- Elmegreen D. M., Elmegreen B. G., 2006, *ApJ*, 651, 676
- Few J. M. A., Madore B. F., 1986, *MNRAS*, 222, 673
- Forbes J., Krumholz M., Burkert A., 2012, *ApJ*, 754, 48
- Förster Schreiber N. M., Shapley A. E., Erb D. K., Genzel R., Steidel C. C., Bouché N., Cresci G., Davies R., 2011a, *ApJ*, 731, 65
- Förster Schreiber N. M. et al., 2011b, *ApJ*, 739, 45
- Förster Schreiber N. M. et al., 2018, *ApJS*, 238, 21
- Förster Schreiber N. M. et al., 2019, *ApJ*, 875, 21
- Freundlich J. et al., 2013, *A&A*, 553, A130
- Freundlich J. et al., 2019, *A&A*, 622, A105
- Gammie C. F., 2001, *ApJ*, 553, 174
- Genel S. et al., 2012, *ApJ*, 745, 11
- Genzel R. et al., 2008, *ApJ*, 687, 59
- Genzel R. et al., 2013, *ApJ*, 773, 68
- Genzel R. et al., 2014, *ApJ*, 785, 75
- Genzel R. et al., 2017, *Nature*, 543, 397
- Genzel R. et al., 2020, preprint ([arXiv:2006.03046](https://arxiv.org/abs/2006.03046))
- Goldbaum N. J., Krumholz M. R., Forbes J. C., 2015, *ApJ*, 814, 131
- Goldbaum N. J., Krumholz M. R., Forbes J. C., 2016, *ApJ*, 827, 28
- Goldreich P., Lynden-Bell D., 1965, *MNRAS*, 130, 97
- Guo Y. et al., 2015, *ApJ*, 800, 39
- Guo Y. et al., 2018, *ApJ*, 853, 108
- Habouzit M. et al., 2019, *MNRAS*, 484, 4413
- Huertas-Company M. et al., 2018, *ApJ*, 858, 114
- Immeli A., Samland M., Gerhard O., Westera P., 2004, *A&A*, 413, 547
- Inoue S., Dekel A., Mandelker N., Ceverino D., Bournaud F., Primack J., 2016, *MNRAS*, 456, 2052
- Jiang F. et al., 2019, *MNRAS*, 488, 4801
- Kennicutt R. C., Jr, 1998, *ARA&A*, 36, 189
- Kennicutt R. C., Jr et al., 2009, *ApJ*, 703, 1672
- Kereš D., Katz N., Weinberg D. H., Davé R., 2005, *MNRAS*, 363, 2
- Kereš D., Katz N., Fardal M., Davé R., Weinberg D. H., 2009, *MNRAS*, 395, 160
- Kravtsov A. V., Klypin A. A., Khokhlov A. M., 1997, *ApJS*, 111, 73
- Krumholz M., 2017, *Star Formation*, World Scientific Series in Astrophysics, World Scientific Publishing Co. Pte. Ltd.
- Krumholz M. R., Dekel A., McKee C. F., 2012, *ApJ*, 745, 69
- Lee B. et al., 2018, *ApJ*, 853, 131
- Lynds R., Toomre A., 1976, *ApJ*, 209, 382
- McMullin J. P., Waters B., Schiebel D., Young W., Golap K., 2007, in Shaw R. A., Hill F., Bell D. J., eds, ASP Conf. Ser. Vol. 376, CASA Architecture and Applications. Astron. Soc. Pac., San Francisco, p. 127
- Mandelker N., Dekel A., Ceverino D., Tweed D., Moody C. E., Primack J., 2014, *MNRAS*, 443, 3675
- Mandelker N., Dekel A., Ceverino D., DeGraf C., Guo Y., Primack J., 2017, *MNRAS*, 464, 635
- Mantha K. B. et al., 2019, *MNRAS*, 486, 2643
- Mapelli M., Moore B., Giordano L., Mayer L., Colpi M., Ripamonti E., Callegari S., 2008a, *MNRAS*, 383, 230
- Mapelli M., Moore B., Ripamonti E., Mayer L., Colpi M., Giordano L., 2008b, *MNRAS*, 383, 1223
- Martig M., Bournaud F., Teyssier R., Dekel A., 2009, *ApJ*, 707, 250
- Martin D. C. et al., 2019, *Nat. Astron.*, 3, 822
- Neistein E., Dekel A., 2008, *MNRAS*, 388, 1792
- Nelson E. J. et al., 2012, *ApJ*, 747, L28
- Newman A. B., Ellis R. S., Treu T., Bundy K., 2010, *ApJ*, 717, L103
- Noguchi M., 1998, *Nature*, 392, 253
- Noguchi M., 1999, *ApJ*, 514, 77
- Ocvirk P., Pichon C., Teyssier R., 2008, *MNRAS*, 390, 1326
- Pichon C., Pogosyan D., Kimm T., Slyz A., Devriendt J., Dubois Y., 2011, *MNRAS*, 418, 2493
- Renaud F. et al., 2018, *MNRAS*, 473, 585
- Salim S., Fang J., Rich R., Faber S., Thilker D., 2012, *ApJ*, 755, 105
- Shakura N. I., Sunyaev R. A., 1973, *A&A*, 24, 337
- Sheth K. et al., 2008, *ApJ*, 675, 1141
- Simons R. C. et al., 2019, *ApJ*, 874, 59
- Snyder G. F., Lotz J., Moody C., Peth M., Freeman P., Ceverino D., Primack J., Dekel A., 2015a, *MNRAS*, 451, 4290
- Snyder G. F. et al., 2015b, *MNRAS*, 454, 1886
- Solomon P. M., Downes D., Radford S. J. E., Barrett J. W., 1997, *ApJ*, 478, 144
- Stewart K. R., Brooks A. M., Bullock J. S., Maller A. H., Diemand J., Wadsley J., Moustakas L. A., 2013, *ApJ*, 769, 74
- Tacchella S. et al., 2015, *Science*, 348, 314
- Tacchella S., Dekel A., Carollo C. M., Ceverino D., DeGraf C., Lapiner S., Mandelker N., Primack J. R., 2016a, *MNRAS*, 458, 242
- Tacchella S., Dekel A., Carollo C. M., Ceverino D., DeGraf C., Lapiner S., Mandelker N., Primack J. R., 2016b, *MNRAS*, 457, 2790
- Tacchella S. et al., 2018, *ApJ*, 859, 56
- Theys J. C., Spiegel E. A., 1977, *ApJ*, 212, 616
- Tollet É., Cattaneo A., Macciò A. V., Dutton A. A., Kang X., 2019, *MNRAS*, 485, 2511
- Tomasetti M. et al., 2016, *MNRAS*, 458, 4477
- Toomre A., 1978, in Longair M. S., Einasto J., eds, Proc. IAU Symp. Vol. 79, Large Scale Structures in the Universe. Kluwer, Dordrecht, p. 109
- van der Wel A. et al., 2014, *ApJ*, 792, L6
- van Dokkum P. G. et al., 2008, *ApJ*, 677, L5
- van Dokkum P. G. et al., 2010, *ApJ*, 709, 1018
- van Dokkum P. G. et al., 2014, *ApJ*, 791, 45
- van Dokkum P. G. et al., 2015, *ApJ*, 813, 23
- Whitaker K. E., Kriek M., van Dokkum P. G., Bezanson R., Brammer G., Franx M., Labb   I., 2012, *ApJ*, 745, 179
- White S. D. M., 1984, *ApJ*, 286, 38
- Williams C. C. et al., 2014, *ApJ*, 780, 1
- Williams C. C. et al., 2015, *ApJ*, 800, 21
- Yuan T. et al., 2020, preprint ([arXiv:2005.11880](https://arxiv.org/abs/2005.11880))
- Zhang H. et al., 2019, *MNRAS*, 484, 5170
- Zolotov A. et al., 2015, *MNRAS*, 450, 2327

SUPPORTING INFORMATION

Supplementary data are available at [MNRAS](#) online.

Table A1. Relevant global properties of the VELA 3 galaxies.

Figure B1. Distribution of ring properties for the significant rings in the simulations, $\mu_{\text{ring}} > 0.3$.

Figure B2. 2D distributions of ring fractions for the simulated galaxies in bins within the $M_v - z$ plane, complementing Fig. 12.

Figure B3. Same as Fig. 12, the distribution of ring fraction for significant rings with $\mu_{\text{ring}} > 0.3$, but in the plane $M_s - z$, for easier comparison to observations.

Figure C1. Evolution of shape ($e - f$, see the text) of the stellar system (blue) as a function of stellar mass for stacked VELA simulated galaxies (median and 1σ scatter).

Figure D1. Evolution from compaction through a blue-nugget to post-blue-nugget disc and ring, complementing Fig. 4.

Figure D2. Mock *HST* three-colour images of simulated galaxies.

Figure D3. Observed rings in three colours.

Please note: Oxford University Press is not responsible for the content or functionality of any supporting materials supplied by the authors. Any queries (other than missing material) should be directed to the corresponding author for the article.

This paper has been typeset from a $\text{\TeX}/\text{\LaTeX}$ file prepared by the author.